Exploring accumulation-mode-H₂SO₄ versus SO₂ stratospheric sulfate geoengineering in a sectional aerosol-chemistry-climate model

Sandro Vattioni[1,2], Debra Weisenstein[2], David Keith[2], Aryeh Feinberg[1], Thomas Peter[1], Andrea Stenke[1]

[1]Institute of Atmospheric and Climate Science, ETH Zürich, Zurich, 8002, Switzerland
[2]Harvard John A. Paulson School of Engineering and Applied Sciences, Cambridge, MA-02138, USA

Correspondence to: Sandro Vattioni (sandro.vattioni@outlook.com)

Abstract. Stratospheric sulfate geoengineering (SSG) could contribute to avoiding some of the adverse impacts of climate change. We used the global 3D-aerosol-chemistry-climate model, SOCOL-AER, to investigate 21 different SSG scenarios, each with 1.83 Mt S yr^{-1} (corresponding to a quarter of the Pinatubo eruption each year) injected either in the form of accumulation-mode-H$_2$SO$_4$ droplets (AM-H$_2$SO$_4$), gas-phase SO$_2$, or as combinations of both. For most scenarios, the sulfur was continuously emitted at 50 hPa ($\approx$ 20 km) altitude in the tropics and subtropics, zonally and latitudinally symmetric about the equator (ranging from $\pm3.75°$ to $\pm30°$). In the SO$_2$ emission scenarios, continuous production of tiny nucleation mode particles results in increased coagulation, which together with gaseous H$_2$SO$_4$ condensation produces coarse mode particles. These large particles are less effective for backscattering solar radiation and sedimentation out of the stratosphere is faster than for AM-H$_2$SO$_4$. On average, AM-H$_2$SO$_4$ injection increases stratospheric aerosol residence times by 32 % and stratospheric aerosol burdens 37-41 % when comparing to SO$_2$ injection. The modelled all-sky (clear-sky) shortwave radiative forcing for AM-H$_2$SO$_4$ injection scenarios is up to 17-70 % (44-57 %) larger than is the case for SO$_2$. Aerosol burdens have a surprisingly weak dependence on the latitudinal spread of emissions with emission in the stratospheric surf zone (> 15° N-15° S) decreasing burdens by only about 10 %. This is because the faster removal through stratosphere-to-troposphere transport via tropopause folds found when injection is spread farther from the equator is roughly balanced by a decrease in coagulation. Increasing injection altitude is also surprisingly ineffective because the increase in global burden is compensated by an increase in large aerosols due to increased condensation and/or coagulation. Increasing the local SO$_2$ flux in the injection region by pulse or point emissions reduces the total global annual nucleation. Coagulation is also reduced due to the interruption of the continuous flow of freshly formed particles. The net effect of pulse or point emission of SO$_2$ is to increase stratospheric aerosol residence time and radiative forcing. Pulse or point emissions of AM-H$_2$SO$_4$ has the opposite effect—decreasing stratospheric aerosol burden and radiative forcing by increasing coagulation. In summary, this study corroborates previous studies with uncoupled aerosol and radiation modules, suggesting that, compared to SO$_2$ injection, the direct emission of AM-H$_2$SO$_4$ results in more radiative forcing for the same sulfur equivalent mass injection strength and that sensitivities to different injection strategies may vary for different forms of injected sulfur.

1 Introduction

Driven by human emissions, long-lived atmospheric greenhouse gas (GHG) concentrations now exceed levels ever experienced by *Homo sapiens*. The effects of these GHGs—as written by the Intergovernmental Panel on Climate Change in 2014—"have been detected throughout the climate system and are extremely likely to have been the dominant cause of the

5 observed warming since the mid-20th century" (IPCC, 2014). Emissions of CO_2 and other GHGs must be curbed to reduce the impacts of climate change. Yet, the long lifetime of CO_2 and some other GHGs suggest that even if emissions were eliminated today, climate change and resulting human and environmental risks would persist for centuries.

We might bring global warming to a halt or reduce its rate of growth by combining emissions cuts with other interventions, such as a deliberate increase in the Earth's stratospheric aerosol burden, which would enhance the albedo of

10 the stratospheric aerosol layer and reduces solar climate forcing. This idea, now often called "solar geoengineering", "solar climate engineering" or "solar radiation management", was first proposed by Budyko (1977) who suggested injecting sulfate aerosols into the stratosphere to increase Earth's albedo. Research on this topic became tabooed because of the entailed risks. However, efforts were renewed after Crutzen (2006) suggested that solar radiation management might be explored as a useful climate change mitigation tool, since adequate emission reductions were becoming increasingly unlikely.

15 Most research on solar geoengineering has focused on stratospheric sulfate geoengineering (SSG) through SO_2 injection, in part due to its volcanic analogues such as the 1991 eruption of Mt. Pinatubo. Studies of SSG, however, have found limitations with SO_2 injection as a method of producing a radiative forcing (RF) perturbation. Limitations include: (1) reduced efficacy at higher loading, limiting the achievable short-wave radiative forcing (Heckendorn et al., 2009; Niemeier et al., 2011; English et al., 2012; Kleinschmitt et al., 2018), (2) depletion of stratospheric ozone (Tilmes et al., 2008;

20 Heckendorn et al., 2009), (3) stratospheric heating (Heckendorn et al., 2009; Ferraro et al., 2011), especially in the tropical lower stratosphere, which would modify the Brewer-Dobson circulation and increase stratospheric water vapor, and (4) enhanced diffuse light at the Earth's surface with repercussions for ecosystems (Kravitz et al., 2012). Limitation (1) is primarily a function of the sulfate particle size distribution, determining their gravitational removal, whereas (2) to (4) are primarily dependent on chemical and radiative particle properties.

25 The size distribution problem with SO_2 injection arises after oxidation of SO_2 to H_2SO_4 when aerosol particles are formed through nucleation and condensation. Condensation onto existing particles increases their average size. In addition, the continuous flow of freshly nucleated particles leads to coagulation, both through self-coagulation of the many small new particles and—more importantly—coagulation with already existing bigger particles from the background aerosol layer. These particles then grow further through coagulation and condensation, which increases the average sedimentation velocity

30 of the aerosol population (Heckendorn et al., 2009). Mean particle sizes tend to increase with the SO_2 injection rate, reducing the stratospheric aerosol residence time and, hence, their radiative forcing efficacy (e.g., W m^{-2} (Mt S yr^{-1})$^{-1}$). This problem could be reduced—and the radiative efficacy increased—if there was a way to produce additional accumulation mode (0.1-1.0 μm radius) sulfate particles (AM-H_2SO_4). Such particles are sufficiently large to decrease their mobility and hence their

coagulation. Furthermore, such particles are close to the radius of maximum mass specific up-scattering of solar radiation on sulfate particles, which is ~0.3 µm (Dykema et al., 2016). One proposed method of doing this is to directly inject H_2SO_4 vapor into a rapidly expanding aircraft plume during stratospheric flight, which would be expected to lead to the formation of accumulation mode particles with a size distribution that depends on the injection rate and the expansion characteristics of

5   the plume (Pierce et al., 2010). Two theoretical studies, Pierce et al. (2010) and Benduhn et al. (2016), suggest that appropriate size distributions could be produced in aircraft plumes using this method.

To evaluate a geoengineering approach with AM-H_2SO_4 one needs to study the evolution of aerosol particles after injection of H_2SO_4 vapor into an aircraft wake and the subsequent transport and evolution of the aerosol plume around the globe. This is a problem with temporal scales ranging from milliseconds to years, and spatial scales from millimeters to

10   thousands of kilometers. At present there is no model that could seamlessly handle the entire range. However, the problem can be divided into two separate domains: (a) from injection to plume dispersal, and (b) from plume dispersal to global scale distribution. Each domain has associated uncertainties, but these can be studied separately with different modeling tools: plume dispersion models for (a), and general circulation models (GCMs) or chemistry-climate models (CCMs) for (b).

(a) Plume modeling. The integration of the plume model starts with the production of small particles in a plume

15   from the exit point of the injection nozzle, and ends when the plume has expanded sufficiently so that the loss of particles by coagulation with ambient particles dominates the self-coagulation, whereupon the GCM or CCM becomes the appropriate tool (Pierce et al., 2010). The plume model needs to account for the initial formation of nucleation mode particles by homogeneous nucleation of H_2SO_4 and H_2O vapor and the subsequent evolution of the particle size distribution by coagulation of the nucleation mode, as well as by condensation of H_2SO_4 vapor on already existing particles. In an

20   expanding aircraft plume, these processes occur on timescales from milliseconds to hours, and length scales from millimeters to kilometers. This was addressed by Pierce et al. (2010) and then by Benduhn et al. (2016). There is rough agreement that particles of 0.095-0.15 µm radius could be produced after the initial plume processing, but these results are subject to uncertainties and need further investigation.

(b) General circulation modeling. The second part of the problem can be analyzed by a GCM or a CCM, starting

25   from the release of sulfate particles of the size distribution calculated by the plume model into the grid of the GCM, all the way to implications on aerosol burden, radiative forcing, ozone, stratospheric temperature and circulation. To this end, the GCM must be coupled to chemistry and aerosol modules. The GCM then provides solutions on how the new accumulation mode particles change the large-scale size distribution, and thus the overall radiative and dynamical response to sulfate aerosol injection. Missing in this methodology are processes smaller than the grid size of the GCM, which may involve

30   filaments of injected material being transported in thin layers. Consideration of these sub-grid scale processes remains an uncertainty of our study, but might be handled by a Lagrangian transport model in a future study.

A sectional (i.e. size-bin resolved) aerosol module is important for a mechanistic understanding of the factors that determine the size distributions of the aerosols. Sectional aerosol models handle the aerosols in different size bins (40 in

SOCOL-AER) whereas modal models usually only apply 3 modes (e.g. Niemeier et al., 2011; Tilmes et al., 2017), each with different r_m and σ, to describe the aerosol distribution. Therefore, the degrees of freedom among modal models usually vary between 4 and 8, whereas there are 40 for a sectional model like SOCOL-AER. Thus, sectional aerosol models represent aerosol distributions with better accuracy, though numerical diffusion does result from the discretization in size space. Two

5   earlier studies of SSG modelling, Heckendorn et al. (2009) and Pierce et al. (2010), used the AER-2D chemistry-transport-aerosol model with sectional microphysics (Weisenstein et al., 1997, 2007). Although the sectional aerosol module within has high size resolution, this 2D model only has a limited spatial resolution with simplified dynamical processes. Two GCM model studies of SSG have used sectional aerosol modules, namely English et al. (2012) and Kleinschmitt et al. (2018). English et al. (2012) used the GCM WACCM (Garcia et al., 2007) coupled to the sectional aerosol module CARMA (Toon

10   et al., 1988) to simulate various SSG scenarios with sulfur emissions in the form of SO_2-gas, H_2SO_4-gas and $AM-H_2SO_4$, but without treatment of the quasi biennial oscillation (QBO) and without online interaction between aerosols, chemistry and radiation. Kleinschmitt et al. (2018) used the GCM LMDZ (Hourdin et al., 2006, 2013) which was coupled to the sectional aerosol module S3A (Kleinschmitt et al., 2017) to simulate various SO_2 emission scenarios, but without injection of AM–H_2SO_4. In their model setup, the aerosols were fully interactive with the radiative scheme, but the model included only

15   simplified chemistry and a prescribed SO_2-to-H_2SO_4 conversion rate.

There have been prior studies with other advanced interactive GCMs, but using modal aerosol schemes. Niemeier et al. (2011) looked at SO_2 and H_2SO_4 gas injection by using the GCM MA-ECHAM coupled to the modal aerosol module HAM (Stier et al., 2005). However, the radiation scheme did not interact with the aerosol module and the chemistry was simplified using prescribed OH concentrations and without ozone chemistry. Mills et al. (2017) and Tilmes et al., (2017)

20   used the fully coupled global chemistry-climate model CESM1 (Hurrell et al., 2013) to simulate SO_2 emission scenarios. In their model setup, they applied higher horizontal and vertical resolutions compared to SOCOL-AER as well as a fully coupled ocean module and more complex chemistry. However, they also relied on a modal aerosol module, which in turn was coupled to cloud microphysics.

In this study we investigate different SO_2 and $AM-H_2SO_4$ emission scenarios by using the sectional global 3D

25   aerosol-chemistry-climate model SOCOL-AER (Sheng et al., 2015), which treats prognostic transport as well as radiative and chemical feedbacks of the aerosols online in one models. As described above, GCMs are not yet able to interactively couple plume dispersion models. Hence, we follow Pierce et al., 2010 and use a log-normal distribution for the injected aerosols in the $AM-H_2SO_4$ emission scenarios. SO_2 emission scenarios are performed as a reference, and to gain insight into aerosol formation processes on a global scale. We perform a number of sensitivity studies with both SO_2 and $AM-H_2SO_4$ that

30   highlight differences between the two injection strategies and indicate future research needs.

2 Model Description

We use the global 3D aerosol-chemistry-climate model SOCOL-AER (Sheng et al., 2015) in this study. An earlier geoengineering study by Heckendorn et al. (2009) used SOCOLv2 (Egorova et al., 2005; Schraner et al., 2008) to study the stratospheric response to SO_2 injections. In that case, the AER–2D model (Weisenstein et al., 1997, 2007) was used to

5   calculate global aerosol properties, which were prescribed in the 3D chemistry-climate model SOCOLv2. The SOCOL-AER (Sheng et al., 2015; Sukhodolov et al., 2018) model is based on SOCOLv3 (Stenke et al., 2013), and improves on the earlier versions of SOCOL by incorporating a sectional aerosol module based on the AER-2D model.

SOCOL-AER includes the chemistry of the sulfate precursors H_2S, CS_2, dimethyl sulfide (C_2H_6S, DMS), OCS, methanesulfonic acid (CH_4O_3S, MSA), SO_2, SO_3, and H_2SO_4, as well as the formation and evolution of particulates via

10   particle size resolving microphysical processes such as homogeneous bimolecular nucleation of H_2SO_4 and H_2O, condensation and evaporation of H_2SO_4 and H_2O, coagulation and sedimentation. As opposed to an earlier version of SOCOL-AER that used a wet radius binning scheme (Sheng et al., 2015), this model version separates the aerosol according to H_2SO_4 mass in 40 bins, with H_2SO_4 mass doubling between neighbouring bins. The new binning approach allows for more accurate consideration of size distribution changes caused by evaporation and condensation of H_2O on the sulfate aerosols.

15   Depending on the grid-box temperature and relative humidity, wet aerosol radii in the new scheme can range from 0.4 nm to 7 µm. Nevertheless, to simplify post-processing of results the sulfate aerosols are rebinned into the original wet size bins of Sheng et al. (2015). SOCOL-AER interactively couples the aerosol module AER with the chemistry module MEZON (Rozanov et al., 1999, 2001; Egorova et al., 2001, 2003) via photochemistry of the sulfate precursor gases as well as heterogeneous chemistry on the particle surfaces. In SOCOL-AER, MEZON treats 56 chemical species of oxygen, nitrogen,

20   hydrogen, carbon, chlorine, bromine and sulfur families with 160 gas phase reactions, 58 photolysis reactions, and 16 heterogeneous reactions, representing the most relevant aspects of stratospheric chemistry. SOCOL-AER also treats tropospheric chemistry, though with a reduced set of organic chemistry (isoprene as most complex organic species), and prescribed aerosols (other than sulfate aerosols, which are fully coupled). SOCOL-AER also interactively couples AER with the general circulation model ECHAM5.4 (Manzini et al., 1997; Roeckner et al., 2003, 2006) of SOCOLv3 via the radiation

25   scheme. SOCOL-AER treats 6 short-wave (SW) radiation bands (185 nm-4 µm) and 16 long-wave radiation bands (4 µm-1 mm) which respond to the aerosol module via the aerosol radiative feedbacks. The extinction coefficients, which are required for each of the 22 wavelengths, as well as the single scattering albedo and the asymmetry factors, which are only taken into account for the 6 short-wave bands, are calculated from the particle size distribution of the 40 size bins according to Mie scattering theory (Biermann et al., 2000), with radiative indexes from Yue et al. (1994). The transport of the sulfur

30   gas species and the aerosol bins is integrated into the advection scheme of ECHAM5 (Lin and Rood, 1996). MEZON is interactively coupled to ECHAM5 using the three-dimensional fields of temperature, wind and radiative forcing of water vapor, methane, ozone, nitrous oxide and chlorofluorocarbons.

Operator splitting is used, whereupon transport is calculated every 15 minutes, and chemistry, microphysics and radiation are calculated every 2 hours, with 3-minute sub-timesteps for microphysical processes. We used T31 horizontal truncation (i.e. 3.75° resolution in longitude and latitude) with a vertical resolution of 39 hybrid sigma-p levels from the surface up to 0.01 hPa (i.e. about 80 km altitude). This results in a vertical resolution of about 1.5 km in the lower

5   stratosphere.

This study is among the first modelling studies on SSG which couple a size-resolved sectional aerosol module interactively to well-described stratospheric chemistry and radiation schemes in a global three-dimensional chemistry-climate model. Furthermore, this study explores the injection of $AM-H_2SO_4$ in detail and contrasts the resulting atmospheric effects and sensitivities with those of gaseous SO_2 injections.

10   **3. Experimental Setup**

In this study, 21 different injection scenarios with annual emissions of 1.83 Mt of sulfur per year (Mt S yr^{-1}) in the form of $AM-H_2SO_4$ (sulfate aerosols) or gaseous SO_2 were performed, as well as runs with mixtures of both species. Per year, this correspond to about one quarter of the sulfur emitted during the Mt. Pinatubo eruption. See Table 1 for a complete list of scenarios. Additionally, a reference run (termed "BACKGROUND") without artificial sulfur emissions was conducted to

15   enable comparison with background conditions. Natural and anthropogenic emissions of chemical species were treated as described by Sheng et al. (2015). Each simulation was performed for 20 years representing atmospheric conditions of the years 2030–2049 for ozone depleting substances (2.3 ppb Cl_Y and 18 ppt Br_Y above 50 km altitude, WMO, (2008)) and greenhouse gas concentrations following the representative concentration pathway 6.0 scenario (RCP6.0), with the first 10 years used as spin-up and the last 10 years used for analysis. Sea surface temperatures (SST) and sea ice coverage (SIC)

20   were prescribed as a repetition of monthly means of the year 2001 from the Hadley Centre Sea Ice and Sea Surface Temperature 1 data set (hadISST1) by the UK Met Office Hadley Centre (Rayner et al., 2003). The QBO was nudged by a linear relaxation of the simulated zonal winds in the equatorial stratosphere to observed wind profiles of the years 1999 and 2000 in a repeating two-year cycle. The geoengineering emissions were injected at 50 hPa altitude (≈ 20 km) except for runs number 19 (termed "GEO_AERO_25km_15") and 20 (termed "GEO_SO2_25km_15") which emitted $AM-H_2SO_4$ and SO_2,

25   respectively, at about 24 hPa altitude (≈ 25 km) to investigate the sensitivity to the emission altitude.

$AM-H_2SO_4$ emissions were parameterized as a log-normal distribution with a dry mode radius (r_m) of 0.095 µm and a distribution width (σ) of 1.5. This is the resulting size distribution determined by Pierce et al. (2010) from a plume model, derived at the point when coagulation with the larger background sulfate particles became dominant over self-coagulation. We also performed one run (number 21, termed "GEO_AERO_radii_00") with a mean radius of 0.15 µm to investigate the

30   sensitivity of aerosol burden and radiative forcing to the initial $AM-H_2SO_4$ size distribution.

Runs 1 to 6 injected $AM-H_2SO_4$ while runs 7 to 12 injected SO_2 at the equator (i.e. ±3.75° N and S), from 5° N to 5° S, 10° N to 10° S, 15° N to 15° S, 20° N to 20° S and from 30° N to 30° S, each uniformly spread over all longitudes.

Emission into the tropical and subtropical stratosphere was chosen to achieve global spreading via the Brewer-Dobson circulation, and various latitudinal spreads were chosen to investigate sensitivity of emitting partly into the surf zone and not only into the tropical pipe. We assumed emission continuous in time, and injected into one vertical model level and the indicated emission area for all the scenarios, except for scenarios 13 and 14 which emitted AM-H_2SO_4 and SO_2, respectively,

5   in two pulses per year (January 1st-2nd and July 1st-2nd of every modelled year) between 10° N and 10° S. Run 15 and 16 are scenarios with emissions into a single equatorial grid box (3.75° x 3.75° in longitude and latitude), whereas all the other scenarios emitted equally at all longitudes around the globe. With these scenarios, we investigated differences between a point source emission (e.g. emissions resulting from a tethered balloon), and equally spread emissions (e.g. emissions from continuously flying planes or a dense grid of continuously operating balloons).

10   We assume that AM-H_2SO_4 is produced in situ in the plumes behind planes which generate SO_3 or H_2SO_4 from burning elemental sulfur. As a 100 % conversion rate is unlikely to be achieved (Smith et al., 2018), we also performed two runs emitting mixtures of SO_2 and AM-H_2SO_4 with only 30 % or 70 % in the form of AM-H_2SO_4 and the rest in the form of SO_2 (runs 17 and 18, respectively).

           Finally, we note that a fully coupled ocean would be desirable to study impacts on tropospheric climate such as

15   surface temperature change. For computational efficiency, we chose not to couple the deep ocean module of SOCOL-AER in the present study. Therefore, we focus on changes in stratospheric aerosol microphysics, chemistry, and changes in surface radiation. We also note particular sensitivities to which horizontal and vertical resolution may play an important role.

4. Results

4.1 The stratospheric sulfur cycle under SSG conditions

20   A simplified representation of the modelled stratospheric sulfur cycle is shown for background conditions and for two geoengineering scenarios in Figure 1. Under background conditions (black numbers in figure), the stratospheric sulfur burden arises primarily from cross-tropopause net fluxes of SO_2 and SO_2 precursor species (OCS, DMS, CS_2 and H_2S) as well as primary tropospheric sulfate aerosols in the rising air masses in the tropics. OCS contributes to the SO_2 burden in the middle stratosphere, while the direct cross-tropopause flux of SO_2 influences mainly the lower stratosphere (Sheng et al.,

25   2015). In the tropical stratosphere, the mean stratospheric winds disperse sulfur species readily in east-west directions, whereas meridional transport is determined by large-scale stirring and mixing through the edge of the tropical pipe at typical latitudes of 15°-20° N and S (Plumb, 1996). Transport into higher latitudes, which occurs mainly via the Brewer−Dobson circulation (Brewer, 1949; Dobson, 1956), results in a stratospheric aerosol residence time (= stratospheric burden divided by net flux to the troposphere) of about 13 months for background conditions in SOCOL-AER (see Table 2). After

30   decomposition of sulfate precursors to SO_2 and subsequent oxidation to H_2SO_4 vapor, sulfate aerosol particles are forming via bimolecular nucleation with H_2O or grow through condensation onto already existing aerosol particles. Condensation is

proportional to the available surface area of pre-existing aerosols and nucleation is mainly a function of temperature and H_2SO_4 partial pressure. The resulting stratospheric aerosol burden differs in some details (~16 % larger total stratospheric aerosol mass) from the one simulated in Sheng et al. (2015) due to different temporal sampling of model output as well as subsequent model updates and development.

5   The aerosol burden resulting from geoengineering AM-H_2SO_4 injection for scenario GEO_AERO_15 (blue) is about 41.4 % larger than the aerosol burden resulting from the equivalent SO_2 injection for scenario GEO_SO2_15 (red). The chemical lifetime of SO_2 in the lower stratosphere varies between 39 to 46 days among our SO_2 emission scenarios (about 35 days for background conditions). The SO_2 injection from GEO_SO2_15 results in an averaged stratospheric SO_2 burden of 222.4 Gg S for steady state conditions, which is 12.8 % of the combined stratospheric SO_2 and aerosol burden.

10 This is a significant fraction compared to the 0.6 % in AM-H_2SO_4 emission scenarios. Especially when considering that the sulfur becomes only "useful" for SSG after transformation to sulfate aerosols. In SO_2 emission scenarios only 4.7 % of the total emitted SO_2 is transported back to the troposphere unprocessed via diffusion and mixing due to tropopause folds at the edges of the tropical pipe. The other 95.3 % of the annually emitted SO_2 is subsequently oxidized to H_2SO_4 of which 37 % nucleates to form new particles and 63 % condenses onto already existing particles. Compared to background conditions,

15 GEO_AERO_15 shows a shift in the processing from nucleation to condensation due to the increased surface area availability. Both SSG scenarios show an increased OCS flux across the tropopause (about +7 % among all scenarios) when comparing to the background run, which indicates that upward mass fluxes across the tropical tropopause are enhanced under SSG conditions. Table 2 lists averaged values of aerosol burden, short-wave radiative forcing, and other quantities for all scenarios modelled, while Table 3 provides the quantities normalized by the corresponding all sky short-wave radiative

20 forcing.

      The SO_2 injection case produces both more nucleation mode (i.e. < 0.01 µm radius) particles and more coarse mode (>1 µm radius) particles than the AM-H_2SO_4 case (see Figure 2). GEO_SO2_15 shows about 3 orders of magnitude higher number concentrations of large particles in the coarse mode compared to GEO_AERO_15. The high concentration of tiny nucleation mode particles (about 4 orders of magnitudes higher compared to BACKGROUND) is due to the large nucleation

25 rate driven by H_2SO_4 gas formed from SO_2 oxidation in GEO_SO2_15. The increase in coarse mode particles is partly due to H_2SO_4 condensing onto existing aerosols, and partly due to increased continuous coagulation of freshly formed nucleation mode particles with larger particles. The larger concentration of coarse mode particles in SO_2 emission scenarios leads to increased aerosol sedimentation rates and thus to about 23.3 % shorter stratospheric aerosol residence times compared to AM-H_2SO_4 emission scenarios. We also show the 5th moment of the aerosol size distribution (see Figure 2, c), which gives

30 an estimate of the downward mass flux due to aerosol sedimentation. This shows that particles in the size range 0.4-1.5 µm are contributing the most to sedimentation in the GEO_SO2_15 scenario. Together with the SO_2 that gets lost to the troposphere unprocessed (4.7 %), the difference in the stratospheric aerosol residence time (32.0 %) explains the biggest part of the total difference of 39.6 % in stratospheric aerosol burden between SO_2 and AM-H_2SO_4 emission scenarios.

In the AM-H_2SO_4 case, the number concentration of nucleation mode particles decreases below background conditions due to the increased surface area for condensation (see Figure 2). For particles larger than 10 nm radius, the simulated distribution in the tropics is similar to the injected aerosol distribution with a peak of about 100 particles per cm^3 at about 0.1 µm radius. In Figure 2, the size range between 0.12 µm and 0.40 µm is highlighted in green as the range in

5 which the efficacy of backscattering solar radiation on sulfate aerosols is at least 70 % of its peak value at 0.3 µm (solid green line, Dykema et al., 2016). In the tropics, the mass fraction of particles in the 0.12 to 0.40 µm size range is 0.79 of the total tropical aerosol mass for GEO_AERO_15 and 0.60 for GEO_SO2_15 (see also Table 3). Coagulation and sedimentation during transport to higher latitudes reduces the overall particle concentration in higher latitudes (dashed curves in Fig. 2) while increasing the mean particle size. Subsequently, the peak at about 0.1 µm in the tropics in

10 GEO_AERO_15 becomes less pronounced and shifts slightly towards larger particles, which is closer to the radius of maximal backscattering of solar radiation on sulfate aerosols. Among all scenarios, the mass fraction in the optimal size range between 0.12 µm and 0.40 µm radius increases with transport to higher latitudes (e.g. 0.86 for GEO_AERO_15 and 0.67 for GEO_SO2_15 between 40° N and 60° N), which results in larger radiative forcing efficiency per stratospheric aerosol burden (see Fig. 2 and Table 3). Overall, AM-H_2SO_4 emission scenarios result in a more favourable aerosol size

15 distributions, with more particles in the optimal size range for backscattering solar radiation compared to SO_2 emission scenarios.

The more favourable size distribution in AM-H_2SO_4 emission scenarios is also illustrated by values of effective radius (r_{eff}) for different scenarios (Fig. 3 and Table 2). The effective radius is the ratio of the 3rd moment to the 2nd moment of the size distribution. The size range between 0.24 µm and 0.36 µm, which is the range at which mass specific up-scatter is

20 at least 90% of its peak backscattering efficiency at 0.3 µm is marked stippled in Figure 3. In GEO_AERO_15 (Fig. 3, a) this r_{eff} size range is seen in the lower stratosphere where aerosol mass concentrations are largest. However, GEO_SO2_15 (Fig. 3, d) shows r_{eff} larger than is optimal for backscattering (up to 0.40 µm) in parts of the lower stratosphere. Our values of r_{eff} for SO_2 emission scenarios are somewhat larger than what was computed by Niemeier et al. (2011), who found effective radii of about 0.3 µm in the lower stratosphere when emitting 2 Mt S at 60 hPa and 0.35 µm when emitting 2 Mt S at 30 hPa.

25 **4.2 Sensitivity simulations**

Latitudinal spread of emissions: Previous studies found that the latitude range of emissions was important in determining size distribution and aerosol burden, and thus the resulting short-wave radiative forcing. English et al. (2012) found a 40 % larger aerosol burden when emitting AM-H_2SO_4 between 32° N and 32° S when compared to emitting between 4° N and 4° S. They suggested that this is partly due to reduced aerosol concentrations and thus less coagulation as a result of a more

30 dilute aerosol plume. However, they simultaneously increased the emission altitude, and thus they also state that the increased aerosol burden could partly be due to the increased stratospheric aerosol residence time at higher emission altitude. In contrast, Niemeier and Timmreck (2015) found small decreases in aerosol burden when emitting between 30° N and 30° S

relative to emitting from 5° N to 5° S. They found greater coagulation with more diffuse emissions, and that emission into the surf zone increased cross-tropopause transport of aerosols and SO$_2$, thus resulting in a reduced stratospheric aerosol burden compared to scenarios that emitted SO$_2$ only into the tropical pipe.

We find a small reduction in aerosol burden (<10 %) and short-wave radiative forcing for both AM-H$_2$SO$_4$ and SO$_2$
5 emission scenarios with increased latitudinal spread of the emissions (see Fig. 4). We assume that increased loss of stratospheric aerosols through tropopause folds in the surf zone with broadly spread emissions (>15° N-15° S) is compensated by increased coagulation and sedimentation of aerosols in scenarios which emit only into the tropical pipe.

Sensitivity to emission altitude: The stratospheric aerosol residence time when emitting at 24 hPa (~25 km) is increased 29.1 % and 40.8 % when emitting AM-H$_2$SO$_4$ and SO$_2$ respectively, relative to emitting at 50 hPa (~20 km).
10 Therefore, GEO_AERO_25km_15 and GEO_SO2_25km_15 result in stratospheric aerosol burden of 2761 and 2190 Gg S respectively. In GEO_SO2_25km_15 the loss of unprocessed SO$_2$ to the tropopause is reduced to 2.3 % which is due to the greater distance of emissions from the tropopause and higher OH concentrations with increasing altitude in the stratosphere. However, because of warmer temperatures at higher altitudes in the stratosphere, the nucleation rate decreases and a larger fraction of the H$_2$SO$_4$ gas condenses onto already existing particles (12 % nucleation, 88 % condensation). Therefore,
15 particles tend to grow to even larger sizes and more accumulate in the coarse mode. The mass fraction of particles between 0.12 µm and 0.40 µm is reduced to only 0.41 and the all sky short-wave radiative forcing is only increased by 27 % in magnitude compared to GEO_SO2_15, which is not proportional to the increase in stratospheric aerosol burden (44.3 %). For GEO_AERO_25km_15 the fraction between 0.12 µm and 0.40 µm is only reduced from 0.79 to 0.77. This results in an all sky short-wave radiative forcing increase of 23 % compared to GEO_AERO_15, which is close to the increase in
20 stratospheric aerosol burden (28.6 %). The latitudinal and vertical distribution of the aerosol mass density and the larger aerosol sizes are also seen in values of r$_{eff}$ (Fig. 3c and e). When emitting at 24 hPa, r$_{eff}$ in the tropical lower stratosphere increases from 0.35 µm to 0.52 µm in the SO$_2$ emission case and from 0.23 µm to 0.39 µm in the AM-H$_2$SO$_4$ emission case. Thus, the stippled area in Figure 3c and e (r$_{eff}$ of 0.24 to 0.36 µm) is below and above the lower stratosphere where most aerosol mass is accumulated. Therefore, emitting at 25 km results in less short-wave radiative forcing per resulting
25 stratospheric aerosol burden. Furthermore, aerosol density remains more concentrated in the tropics when emitting at 25 km (see also Fig. 7a and b), due to a less leaky tropical pipe at higher stratospheric altitudes. However, when looking at the resulting clear sky short-wave radiative forcing (Fig. 7c and d), the peak in the tropics is only slightly increased in the SO$_2$ emission case and is even lower than the equivalent emission scenario at 20 km in the AM-H$_2$SO$_4$ emission case.

Sensitivity to the injection mode radius: GEO_AERO_radii_15 released AM-H$_2$SO$_4$ with mean radii of 0.15 µm
30 instead of 0.095 µm. This results in a slightly fewer but larger particles in the emitted aerosol plume. The increased injection radius resulted in slightly reduced aerosol burden due to either different coagulation and condensation regimes or faster sedimentation of the slightly larger particles. However, due to the increase of particles in the optimal size range for backscattering solar radiation (+11 %), the all sky short-wave radiative forcing increased about 20 % compared to

GEO_AERO_15 (see Figure 4). When looking at Tables 2 and 3, there is only a small difference in r_{eff} between the AM-H_2SO_4 emission scenarios with r_m of 0.95 µm and 0.15 µm, indicating only minor dependence of small changes in r_m on the resulting distribution of accumulation mode particles.

Mixtures of AM–H_2SO_4 and SO_2: We also performed calculations to explore the utility of emitting SO_2 and AM-H_2SO_4 together (see Fig. 5). Some studies have suggested that planes carrying elemental sulfur and burning it in situ to directly emit H_2SO_4-gas or AM-H_2SO_4 would be the most effective way to deliver sulfate to the stratosphere (Benduhn et al. 2016, Smith et al. 2018). Burning elemental sulfur would also reduce the freight to be transported to the stratosphere (i.e. 32 g mol^{-1} for sulfur rather than 98 g mol^{-1} for H_2SO_4 or 64 g mol^{-1} for SO_2). However, 100 % conversion to H_2SO_4 is unlikely, with the remainder emitted as SO_2. Our results show that a small portion (30 %) of SO_2 in the emission mixture (i.e.

10 GEO_70%AERO_15) leads only to a slight reduction in the resulting stratospheric aerosol burden (-7 %) as well as in the mass fraction in the optimal size range for backscattering solar radiation (see Table 2 and 3). And that a small portion (30 %) of AM-H_2SO_4 in an emission mixture dominated by SO_2 (i.e. GEO_30%AERO_15) can increase stratospheric aerosol burden and short-wave radiative forcing significantly with respect to a pure SO_2 emission scenario (GEO_SO2_15). As the decrease in efficiency with increasing SO_2 portion in the emission mixture is strongly non-linear in our simulations, we do

15 not expect significant efficiency loss for small portions of SO_2 in the emissions after in situ burning of elemental sulfur in planes.

Spatio-temporal spread of emissions: Emitting AM-H_2SO_4 in two pulses per year as assumed in GEO_AERO_pulsed_10 decreases the stratospheric aerosol burden by about 5 % compared to the continuous emission scenario, GEO_AERO_10. This is due to the ~91 times larger aerosol mass concentration in the emission plume compared to

20 GEO_AERO_10 (emission during 4 days per year instead of 365), and thus more coagulation and faster sedimentation. Similar but much smaller effects were observed for GEO_AERO_point_00, which emitted at one equatorial grid box only (3.75° x 3.75°), and thus with 96 times increased mass concentration in the emission region compared to GEO_AERO_00 (emissions spread over 3.75° in longitude instead of 360°). This indicates fast zonal mixing which reduces the effect of the higher initial mass concentration compared to the pulsed emissions.

25 However, looking at GEO_SO2_pulsed_10 and GEO_SO2_point_00, which are the equivalent SO_2 emission scenarios, the stratospheric aerosol burden increased compared to the continuous emission scenarios. This is mainly due to a reduction in the total globally averaged aerosol nucleation rate (23 % nucleation, 77 % condensation) and the subsequent reduction in total coagulation. However, locally for GEO_SO2_point_00 and spatially for GEO_SO2_pulsed_10 the nucleation rates are increased in the emission area due to the greatly increased H_2SO_4 concentration in the emission region in

30 these scenarios. These two scenarios produce spatially/temporally large amounts of nucleation mode particles which then quickly coagulate to produce accumulation mode particles. After dilution when nucleation is small again, the continuous flow of tiny, freshly nucleated particles is disrupted, and coagulation is reduced. Thus, the mean particle diameter is reduced

and the stratospheric aerosol residence time is increased compared to the respective continuous emission scenarios. This process partially mimics what would go on in an SO_2 plume emitted by an aircraft.

4.3 Temperature and H_2O at the tropical cold point tropopause

Increased aerosol burden in the stratosphere also leads to heating of the lower stratosphere, mainly due to absorption of
5 longwave radiation. The longwave surface anomaly is about 0.1 W m^{-2} among all scenarios. Heating of the cold point tropopause results in temperature increases of 0.7 to 1.2 K among all scenarios associated, with an H_2O entry value increase of about 0.30 to 0.55 ppmv (i.e. 9-17 %, see Fig. 6). The increased stratospheric H_2O volume mixing ratio results in an increase of OH volume mixing ratio (H2O+O(^{1}D) => 2 OH), which additionally increases the HO_X-ozone depletion cycle.

Figure 6 (c and d) shows how H_2O volume mixing ratios increase above 200 hPa. The increase is slightly larger for
10 the AM-H_2SO_4 scenarios due to the higher aerosol load and more pronounced heating of the lower stratosphere. However, when comparing the vertical OH profiles (Fig. 4, a and b), the difference in OH between the SO_2 and the AM-H_2SO_4 scenarios increases to about 4 % at about 50 hPa, which is caused by the depletion of OH due to SO_2 oxidation (SO_2+OH=>SO_3 +HO_2).

Kleinschmitt et al. (2018) applied constant climatological SO_2 with a lifetime of 41 days in their study and found a
15 SO_2-to-H_2SO_4 conversion rate of 96 %. They expected a slightly lower concentration in oxidants and therefore a longer SO_2 lifetime when taking chemical interactions into account. However, they did not consider the increased stratospheric H_2O volume mixing ratio under SSG conditions which causes an OH concentration increase of up to 8 %, making stratospheric SO_2 lifetime shorter and not longer.

4.4 AM–H_2SO_4 vs. SO_2 emissions

20 All sky (clear sky) short-wave radiative forcing from AM-H_2SO_4 emission scenarios 1-6 result in an average of 1.31 W m^{-2} (2.24 W m^{-2}) and are 36.4 % (50.3 %) larger compared to the average of the equivalent SO_2 emission scenarios (7-12) which result in 0.96 W m^{-2} (1.49 W m^{-2}). Table 2 summarizes globally averaged quantities of all modelled SSG scenarios. The fifth column shows the ratios between surface clear sky and surface all sky short-wave radiative forcing. These values for the AM-H_2SO_4 emission scenarios are about 10 % larger than for the SO_2 emission scenarios, indicating a larger reduction of
25 short-wave radiative forcing due to clouds and/or chemical interactions among these scenarios. The stratospheric aerosol burdens for the AM-H_2SO_4 scenarios are more concentrated within the tropical pipe between 15° N and 15° S compared to the equivalent SO_2 emission scenarios that are more evenly distributed across all latitudes, as shown in Figure 7a and b. When looking at the clear sky short-wave radiative forcing (Fig. 7 c and d), the tropical peak flattens out compared to the peak in aerosol burden (Fig. 7 a and b) because the up-scattered fraction of solar radiation increases with increasing solar
30 zenith angle. For the SO_2 emission scenarios, the clear sky short-wave radiative forcing is almost equally distributed between 60° N and 60° S, whereas for the AM-H_2SO_4 scenarios, a pronounced peak can still be observed in the tropics where cloud

cover is larger on average. Thus, the higher aerosol mass fraction in the cloudy tropics makes SSG less efficient in these regions. We assume the difference in surface clear sky to surface all sky short-wave radiative forcing ratios to be a result of a more favourable global spread of the resulting stratospheric aerosol burden for SO_2 emission scenarios. However, this indicates that emitting only within the tropical pipe region might not be the optimal setup of SSG studies. Emitting at the

5   edges of the tropical pipe at 15° N and 15° S like that investigated by Tilmes et al. (2017) might be a more efficient way to achieve higher short-wave radiative forcing with fewer negative side effects.

When looking at the depletion of the total ozone column (Fig. 7, e and f), we find larger depletion among the AM-H_2SO_4 emission scenarios. This is mainly due to the larger surface area densities for AM-H_2SO_4 scenarios in the emission region in the tropics where ozone is produced. This leads to larger ozone depletion and therefore less ozone transport to

10   higher latitudes. Therefore, among the AM-H_2SO_4 emissions scenarios, the vertical ozone column is depleted up to 7.5 % (for GEO_AERO_15 and GEO_AERO_00) at the south polar region in a 10-years average, whereas for the SO_2 emission scenarios, it is only up to 6 % (for GEO_SO2_10). The ozone depletion arises through formation of the reservoir species HNO_3 through N_2O_5 hydrolysis on aerosol surfaces which indirectly enhances the ClO_x ozone depletion cycle. Furthermore, chlorine gets activated through the heterogenous reaction of $ClONO_2$ with HCl, which contributes the most to the ozone

15   depletion due to SSG.

Table 3 shows values from Table 2 normalized to the globally averaged all sky short-wave radiative forcing. The smallest absolute values are marked in green and the largest are marked in red. The smaller the absolute values, the larger the short-wave radiative forcing, and the smaller the negative side effects. Green values are accumulated among the AM-H_2SO_4 emission scenarios and red values are accumulated among the SO_2 emission scenarios. Temperature and water vapour

20   increase at the tropical cold point tropopause and global depletion of the ozone column are 13.6 % and 55.3 % larger, respectively, for the AM-H_2SO_4 emission scenarios than for SO_2 emission scenarios when normalizing to the emission rate of 1.83 Mt S yr^{-1}. However, when normalized by the resulting all sky short-wave radiative forcing, the increase in efficiency among the AM-H_2SO_4 emission scenarios outweighs the worse side effects in the AM-H_2SO_4 scenarios.

5. Discussion

25   In this study, the three-dimensional global aerosol-chemistry-climate model SOCOL-AER was used to investigate AM-H_2SO_4 and SO_2 emission scenarios for the purpose of SSG. We analysed the stratospheric sulfur cycle, aerosol burden, short-wave radiative forcing, and stratospheric temperature-H_2O-OH interactions for various SSG scenarios with injection at about 50 hPa (≈ 20 km) altitude and two with injection at about 20 hPa (≈ 25 km) altitude with a sulfur mass equivalent emission rate of 1.83 Mt S yr^{-1} within the tropics and subtropics.

30   Direct emission of aerosol particles in the accumulation mode results in 30-40 % larger stratospheric aerosol burden and short-wave radiative forcing compared to sulfur mass equivalent SO_2 emission scenarios. This difference in burden is mainly because of two reasons. (1) AM-H_2SO_4 emissions have the advantage of demonstrating effects immediately after

emission and not only after more than one month of transport and photochemistry like that of SO_2 emissions (lifetime of SO_2 of 39 to 46 days through oxidation). Thus, direct AM-H_2SO_4 emission can create an immediate, targeted effect over the area of emission, whereas in SO_2 emission scenarios about 12.4 % of the annually emitted sulfur is present in form of SO_2 on average. (2) The size distribution of SO_2 emission scenarios shows coarse mode particle concentrations which are about two

5   orders of magnitudes larger compared to AM-H_2SO_4 emission scenarios. These particles sediment faster and reduce the average stratospheric residence time of the aerosols compared to AM-H_2SO_4 scenarios. In addition, the short-wave radiative forcing in SO_2 emission scenarios is influenced by the smaller mass fraction of particles in the optimal size range for backscattering solar radiation (i.e. 0.3 µm radius). The unfavourable size distribution for sulfate aerosols resulting from SO_2 emissions is largely due to condensation onto existing particles and the pronounced formation of tiny nucleation mode

10   particles which subsequent coagulation with larger aerosols to create coarse mode particles.

Stratospheric aerosol burden and clear sky short-wave radiative forcing are about 10 % higher for scenarios which avoid emitting into the surf zone, i.e. outside 15° N and 15° S. A higher mass fraction of stratospheric aerosol burden in the tropics for AM-H_2SO_4 emission scenarios reduces all sky radiative forcing efficiency due to the higher cloud fraction in the tropics. AM-H_2SO_4 emission scenarios also result in slightly more stratospheric ozone depletion and stratospheric warming.

15   However, due to the larger absolute short-wave radiative forcing, the negative side effects are smaller for AM-H_2SO_4 emission scenarios compared to SO_2 emission scenarios when normalizing to the surface all sky short-wave radiative forcing.

On the one hand, for AM-H_2SO_4 emission scenarios, temporally and spatially increasing the mass density in the emission region leads to slightly shorter aerosol residence times through more coagulation, and thus reduced short-wave radiative forcing. On the other hand, for SO_2 emission scenarios, a larger stratospheric aerosol burden for a fixed sulfur

20   emission rate can be achieved by temporally or spatially increasing the SO2 mass density. This strategy increases nucleation and coagulation rates in the emission region while minimizing nucleation and coagulation on a global scale. The optimal frequency of the pulses as well as optimal spatial extent of the emissions requires further investigation. However, these results indicate a strong dependence on small-scale processes such as locally changing SO_2 and OH mass concentrations (e.g. emissions along the trajectory of an aircraft), which cannot be resolved in GCMs. Furthermore, they underline the

25   importance of interactions between chemistry and aerosols when modelling SSG scenarios.

We found that in the lower stratosphere OH concentrations are increased up to 9 % for AM-H_2SO_4 emission scenarios compared to the background run due to increased temperatures at the tropical cold point tropopause and thus higher water volume mixing ratios in the stratosphere. However, due to oxidation of SO_2 in SO_2 emission scenarios, the OH concentrations are only increased by about 4 % in the lower stratosphere compared to the background run in these scenarios.

30   We also examined scenarios in which mixtures of SO_2 and AM-H_2SO_4 were emitted. Pure AM-H_2SO_4 emission scenarios resulted in the largest stratospheric aerosol burdens as well as the largest clear sky and all sky short-wave radiative forcing. While the short-wave radiative forcing decreases with increasing fractions of SO_2, that increase is non-linear. A small fraction of SO_2 within emissions of AM-H_2SO_4 results in only slightly smaller radiative forcing efficiency, whereas a

small fraction of AM-H_2SO_4 within emissions of SO_2 increases radiative forcing efficiency significantly. In situ burning of elemental sulfur in planes with subsequent conversion to SO_3 and, in the plume to AM-H_2SO_4 particles might therefore be effective in controlling the aerosol size distribution, even if conversion efficiency were significantly less than unity.

We found clear sky short-wave radiative forcing efficiencies of -1.22 W m^{-2} and -0.82 W m^{-2} per emitted Mt of

5   sulfur equivalent injection rate (W m^{-2} (Mt S yr^{-1})$^{-1}$) for AM-H_2SO_4 and SO_2 emissions at 20 km respectively. For all sky radiative forcing, the efficiencies were about -0.72 W m^{-2} and -0.52 W m^{-2} per emitted Mt of sulfur respectively. These values are smaller compared to other models (i.e. ~-0.83 W m^{-2} (Mt S yr^{-1})$^{-1}$for MAECHAM5 emitted as SO_2 in Niemeier et al., (2011), ~-0.70 W m^{-2} (Mt S yr^{-1})$^{-1}$ for LMDZ-S3A emitted as SO_2 in Kleinschmitt et al., (2018)), likely due to differences in transport processes as well as lower stratospheric aerosol burdens in our model. When emitting SO_2 at 25 km

10   altitude the efficiency is -0.56 W m^{-2} (Mt S yr^{-1})$^{-1}$ in SOCOL-AER and -0.61 W m^{-2} (Mt S yr^{-1})$^{-1}$ for MAECHAM5 (Niemeier et al., 2011). On the one hand, this could be partially a result of different sedimentation, coagulation and aerosol binning schemes compared to other aerosol modules. On the other hand, SOCOL-AER slightly overestimates the Brewer–Dobson circulation (Dietmüller et al., 2018), which would result in larger aerosol burdens compared to other models. However, as many processes are non-linear with increasing injection rates, the efficiencies might be different for other

15   injection rates. Due to the lack of atmospheric observations or small-scale field experiments, modelling studies are currently the only method to estimate efficiency and the possible adverse effects of SSG. Therefore, model intercomparison studies should further identify strengths and weaknesses among different models to reduce uncertainty. Furthermore, atmospheric field studies such as the Stratospheric Controlled Perturbation Experiment (SCoPEx, Dykema et al., 2014) could give further insight into stratospheric aerosol formation and plume evolution.

20   Additional uncertainties arise from the rather low resolution applied in this study. In particular, an increase in the vertical resolution as well as treatment of an interactive QBO could further increase the explanatory power of SSG studies with SOCOL-AER. To study tropospheric climate change, ocean feedback would have to be taken into account with the deep ocean module of SOCOL-AER. Furthermore, SOCOL-AER does not treat cloud interactions—which is likely one of the major uncertainties of the model as aerosols may have large impacts on clouds. We only performed scenarios with

25   emission regions limited to the tropics and subtropics centered around the equator. Nevertheless, SOCOL-AER is one of the first models that interactively couples a sectional aerosol module to the well-described chemistry and radiation schemes of a CCM.

This study shows that direct emission of aerosols can give better control of the resulting size distribution, which subsequently results in more effective radiative forcing. Therefore, the SSG modelling community should increase their

30   focus on direct AM-H_2SO_4 emission as well as on the emission of solid particles (Weisenstein et al., 2015), such as calcite particles (Keith et al., 2016). Further investigations using SOCOL-AER to understand adverse effects of SSG, such as a closer look on ozone depletion, impacts on precipitation patterns, or on stratospheric dynamics will be conducted in future

studies. These studies will also include coupling of the deep ocean module of SOCOL-AER to investigate impacts on the tropospheric climate.

Furthermore, we show that interactive coupling of aerosols, chemistry and radiation schemes are essential features for modelling SSG emission scenarios with GCMs. For SO_2 emission scenarios, local depletion of oxidants was found,
5 particularly with large SO_2 mass concentrations in the emission region. Accurate modelling of these scenarios might require higher temporal and spatial resolution than has been achieved among current GCMs. Therefore, coupling of small-scale Lagrangian plume dispersion models which simulate the first few days of aerosol-chemistry interactions and aerosol microphysics in evolving emission plumes from airplanes might be a desirable tool to improve future SSG modelling studies. This would appropriately account for the problem of connecting small scale temporal and spatial processes—such as aerosol
10 formation, growth and evolution in an aircraft wakes—to the larger grid of GCMs, which has been neglected in past SSG studies.

Author Contributions

This paper is a result of the master thesis of Sandro Vattioni to gain his master's degree in atmospheric and climate science at ETH Zürich. The thesis was conducted at Harvard University as an exchange research project with ETH Zürich. The
15 project was initialized by Prof. Thomas Peter, who had the lead of the project. While he provided main supervision on the scientific part of the study, Prof. David Keith provided main supervision on the engineering part. Dr. Andrea Stenke coordinated the whole thesis and had the oversight of the study. The design of the different simulations was elaborated by all the authors under the lead of Prof. David Keith with support from Dr. John Dykema, Dr. Lee Miller and Dr. Pete Irvine. SOCOL-AER that originated from the Peter-group at ETH Zürich was made running on the Harvard cluster by Debra
20 Weisenstein. Together with Dr. Andrea Stenke she also contributed by close supervision of Sandro Vattioni during the whole project. Sandro Vattioni adapted the SOCOL-AER model code for sulfate geoengineering purpose, conducted the simulations and analysed the data, while some precoded material for data analysis was provided by Dr. Andrea Stenke and Debra Weisenstein. Aryeh Feinberg contributed with updating and further development of SOCOL-AER as well as with support on the interpretation of the model output. The first manuscript of the paper was written by Sandro Vattioni. The final
25 paper as well as data interpretation resulted from collective discussions, commenting and editing by all the authors. Financial support and founding for the paper writing process was provided from both, the Keith-group at Harvard University and the Peter-group at ETH Zürich in equal parts.

Acknowledgments

We want to thank Dr. Joshua Klobas and Dr. Jian-Xiong Sheng for the valuable discussions on the SOCOL-AER model. Furthermore, we also want to thank Francesco Pontiggia from the Harvard Research Computing team for his help in getting SOCOL-AER running on the Harvard cluster.

5 **References**

Benduhn, F., Schallock, J. and Lawrence, M. G.: Early growth dynamical implications for the steerability of stratospheric solar radiation management via sulfur aerosol particles, Geophys. Res. Lett., 43(18), 9956–9963, doi:10.1002/2016GL070701, 2016.

Biermann, U. M., Luo, B. P. and Peter, T.: Absorption Spectra and Optical Constants of Binary and Ternary Solutions of
10 H_2SO_4, HNO_3, and H_2O in the Mid Infrared at Atmospheric Temperatures, J. Phys. Chem. A, 104(4), 783–793, doi:10.1021/jp992349i, 2000.

Brewer, A. W.: Evidence for a world circulation provided by the measurements of helium and water vapour distribution in the stratosphere, Q. J. R. Meteorol. Soc., 75(326), 351–363, doi:10.1002/qj.49707532603, 1949.

Budyko, M. I.: On present-day climatic changes, Tellus, 29(3), 193–204, doi:10.1111/j.2153-3490.1977.tb00725.x, 1977.

15 Crutzen, P. J.: Albedo Enhancement by Stratospheric Sulfur Injections: A Contribution to Resolve a Policy Dilemma?, Clim. Change, 77(3), 211, doi:10.1007/s10584-006-9101-y, 2006.

Dai, Z., Weisenstein, D. K. and Keith, D. W.: Tailoring Meridional and Seasonal Radiative Forcing by Sulfate Aerosol Solar Geoengineering, Geophys. Res. Lett., 45(2), 1030–1039, doi:10.1002/2017GL076472, 2018.

Dietmüller, S., Eichinger, R., Garny, H., Birner, T., Boenisch, H., Pitari, G., Mancini, E., Visioni, D., Stenke, A., Revell, L.,
20 Rozanov, E., Plummer, D. A., Scinocca, J., Jöckel, P., Oman, L., Deushi, M., Kiyotaka, S., Kinnison, D. E., Garcia, R., Morgenstern, O., Zeng, G., Stone, K. A. and Schofield, R.: Quantifying the effect of mixing on the mean age of air in CCMVal-2 and CCMI-1 models, Atmospheric Chem. Phys., 18(9), 6699–6720, doi:https://doi.org/10.5194/acp-18-6699-2018, 2018.

Dobson, D. M. B.: A discussion on radiative balance in the atmosphere - Origin and distribution of the polyatomic molecules in the atmosphere, Proc. R. Soc. Lond. Math. Phys. Eng. Sci., 236(1205), 187–193, doi:10.1098/rspa.1956.0127, 1956.

25 Dykema, J., Keith, D., Anderson, J. G. and Weisenstein, D.: Stratospheric controlled perturbation experiment (SCoPEx): a small-scale experiment to improve understanding of the risks of solar geoengineering, Philos. Trans. R. Soc. A, 372, doi:10.1098/rsta.2014.0059, 2014.

Dykema, J. A., Keith, D. W. and Keutsch, F. N.: Improved aerosol radiative properties as a foundation for solar geoengineering risk assessment, Geophys. Res. Lett., 43(14), 7758–7766, doi:10.1002/2016GL069258, 2016.

30 Egorova, T., Rozanov, E., Zubov, V. A. and Karol, I.: Model for investigating ozone trends (MEZON), Izv. - Atmospheric Ocean Phys., 39, 277–292, 2003.

Egorova, T., Rozanov, E., Zubov, V., Manzini, E., Schmutz, W. and Peter, T.: Chemistry-climate model SOCOL: a validation of the present-day climatology, Atmospheric Chem. Phys., 5(6), 1557–1576, doi:10.5194/acp-5-1557-2005, 2005.

Egorova, T. A., Rozanov, E. V., Schlesinger, M. E., Andronova, N. G., Malyshev, S. L., Karol, I. L. and Zubov, V. A.: Assessment of the effect of the Montreal Protocol on atmospheric ozone, Geophys. Res. Lett., 28(12), 2389–2392, doi:10.1029/2000GL012523, 2001.

English, J. M., Toon, O. B. and Mills, M. J.: Microphysical simulations of sulfur burdens from stratospheric sulfur geoengineering, Atmospheric Chem. Phys., 12(10), 4775–4793, doi:10.5194/acp-12-4775-2012, 2012.

Ferraro, A. J., Highwood, E. J. and Charlton-Perez, A. J.: Stratospheric heating by potential geoengineering aerosols, Geophys. Res. Lett., 38(24), doi:10.1029/2011GL049761, 2011.

Garcia, R. R., Marsh, D. R., Kinnison, D. E., Boville, B. A. and Sassi, F.: Simulation of secular trends in the middle atmosphere, 1950–2003, J. Geophys. Res. Atmospheres, 112(D9), doi:10.1029/2006JD007485, 2007.

Heckendorn, P., Weisenstein, D., Fueglistaler, S., Luo, B. P., Rozanov, E., Schraner, M., Thomason, L. W. and Peter, T.: The impact of geoengineering aerosols on stratospheric temperature and ozone, Environ. Res. Lett., 4(4), doi:Artn 045108 10.1088/1748-9326/4/4/045108, 2009.

Hourdin, F., Musat, I., Bony, S., Braconnot, P., Codron, F., Dufresne, J.-L., Fairhead, L., Filiberti, M.-A., Friedlingstein, P., Grandpeix, J.-Y., Krinner, G., LeVan, P., Li, Z.-X. and Lott, F.: The LMDZ4 general circulation model: climate performance and sensitivity to parametrized physics with emphasis on tropical convection, Clim. Dyn., 27(7–8), 787–813, doi:10.1007/s00382-006-0158-0, 2006.

Hourdin, F., Grandpeix, J.-Y., Rio, C., Bony, S., Jam, A., Cheruy, F., Rochetin, N., Fairhead, L., Idelkadi, A., Musat, I., Dufresne, J.-L., Lahellec, A., Lefebvre, M.-P. and Roehrig, R.: LMDZ5B: the atmospheric component of the IPSL climate model with revisited parameterizations for clouds and convection, Clim. Dyn., 40(9), 2193–2222, doi:10.1007/s00382-012-1343-y, 2013.

Hurrell, J. W., Holland, M. M., Gent, P. R., Ghan, S., Kay, J. E., Kushner, P. J., Lamarque, J.-F., Large, W. G., Lawrence, D., Lindsay, K., Lipscomb, W. H., Long, M. C., Mahowald, N., Marsh, D. R., Neale, R. B., Rasch, P., Vavrus, S., Vertenstein, M., Bader, D., Collins, W. D., Hack, J. J., Kiehl, J. and Marshall, S.: The Community Earth System Model: A Framework for Collaborative Research, Bull. Am. Meteorol. Soc., 94(9), 1339–1360, doi:10.1175/BAMS-D-12-00121.1, 2013.

IPCC: Climate Change 2014: Synthesis Report. Contribution of Working Groups I, II and III to the Fifth Assessment Report of the Intergovernmental Panel on Climate Change, , 151, 2014.

Keith, D. W., Weisenstein, D. K., Dykema, J. A. and Keutsch, F. N.: Stratospheric solar geoengineering without ozone loss, Proc. Natl. Acad. Sci. U. S. A., 113(52), 14910–14914, doi:10.1073/pnas.1615572113, 2016.

Kleinschmitt, C., Boucher, O., Bekki, S., Lott, F. and Platt, U.: The Sectional Stratospheric Sulfate Aerosol module (S3A-v1) within the LMDZ general circulation model: description and evaluation against stratospheric aerosol observations, Geosci. Model Dev., 10(9), 3359–3378, 2017.

Kleinschmitt, C., Boucher, O. and Platt, U.: Sensitivity of the radiative forcing by stratospheric sulfur geoengineering to the amount and strategy of the SO2 injection studied with the LMDZ-S3A model, Atmospheric Chem. Phys., 18(4), 2769–2786, doi:10.5194/acp-18-2769-2018, 2018.

Kravitz, B., MacMartin, D. G. and Caldeira, K.: Geoengineering: Whiter skies?: GEOENGINEERING WHITER SKIES, Geophys. Res. Lett., 39(11), L11801, doi:10.1029/2012GL051652, 2012.

Lin, S.-J. and Rood, R. B.: Multidimensional Flux-Form Semi-Lagrangian Transport Schemes, Mon. Weather Rev., 124(9), 2046–2070, doi:10.1175/1520-0493(1996)124<2046:MFFSLT>2.0.CO;2, 1996.

Manzini, E., McFarlane, N. A. and McLandress, C.: Impact of the Doppler spread parameterization on the simulation of the middle atmosphere circulation using the MA/ECHAM4 general circulation model, J. Geophys. Res. Atmospheres, 102(D22), 25751–25762, doi:10.1029/97JD01096, 1997.

Mills, M. J., Richter, J. H., Tilmes, S., Kravitz, B., MacMartin, D. G., Glanville, A. A., Tribbia, J. J., Lamarque, J.-F., Vitt, F., Schmidt, A., Gettelman, A., Hannay, C., Bacmeister, J. T. and Kinnison, D. E.: Radiative and Chemical Response to Interactive Stratospheric Sulfate Aerosols in Fully Coupled CESM1(WACCM), J. Geophys. Res. Atmospheres, 122(23), 13,061-13,078, doi:10.1002/2017JD027006, 2017.

Niemeier, U. and Timmreck, C.: What is the limit of climate engineering by stratospheric injection of SO_2?, Atmospheric Chem. Phys., 15(16), 9129–9141, doi:https://doi.org/10.5194/acp-15-9129-2015, 2015.

Niemeier, U., Schmidt, H. and Timmreck, C.: The dependency of geoengineered sulfate aerosol on the emission strategy, Atmospheric Sci. Lett., 12(2), 189–194, doi:10.1002/asl.304, 2011.

Pierce, J. R., Weisenstein, D. K., Heckendorn, P., Peter, T. and Keith, D. W.: Efficient formation of stratospheric aerosol for climate engineering by emission of condensible vapor from aircraft, Geophys. Res. Lett., 37(18), doi:10.1029/2010GL043975, 2010.

Plumb, R. A.: A tropical pipe model of stratospheric transport, J. Geophys. Res. Atmospheres, 101(D2), 3957–3972, doi:10.1029/95JD03002, 1996.

Rayner, N. A., Parker, D. E., Horton, E. B., Folland, C. K., Alexander, L. V., Rowell, D. P., Kent, E. C. and Kaplan, A.: Global analyses of sea surface temperature, sea ice, and night marine air temperature since the late nineteenth century, J. Geophys. Res. Atmospheres, 108(D14), doi:10.1029/2002JD002670, 2003.

Roeckner, E., Bauml, G., Bonaventura, L., Brokopf, R., Esch, M. and Giorgetta, M.: The atmospheric general circulation model ECHAM 5. PART I: Model description, Rep. Max Plank Inst. Meteorol., 349, 2003.

Roeckner, E., Brokopf, R., Esch, M., Giorgetta, M., Hagemann, S., Kornblueh, L., Manzini, E., Schlese, U. and Schulzweida, U.: Sensitivity of Simulated Climate to Horizontal and Vertical Resolution in the ECHAM5 Atmosphere Model, J. Clim., 19(16), 3771–3791, doi:10.1175/JCLI3824.1, 2006.

Rozanov, E. V., Zubov, V. A., Schlesinger, M. E., Yang, F. and Andronova, N. G.: The UIUC three-dimensional stratospheric chemical transport model: Description and evaluation of the simulated source gases and ozone, J. Geophys. Res. Atmospheres, 104(D9), 11755–11781, doi:10.1029/1999JD900138, 1999.

Rozanov, E. V., Schlesinger, M. E. and Zubov, V. A.: The University of Illinois, Urbana-Champaign three-dimensional stratosphere-troposphere general circulation model with interactive ozone photochemistry: Fifteen-year control run climatology, J. Geophys. Res. Atmospheres, 106(D21), 27233–27254, doi:10.1029/2000JD000058, 2001.

Schraner, M., Rozanov, E., Schnadt Poberaj, C., Kenzelmann, P., Fischer, A. M., Zubov, V., Luo, B. P., Hoyle, C. R., Egorova, T., Fueglistaler, S., Brönnimann, S., Schmutz, W. and Peter, T.: Technical Note: Chemistry-climate model SOCOL: version 2.0 with improved transport and chemistry/microphysics schemes, Atmospheric Chem. Phys., 8(19), 5957–5974, doi:10.5194/acp-8-5957-2008, 2008.

Sheng, J.-X., Weisenstein, D. K., Luo, B.-P., Rozanov, E., Stenke, A., Anet, J., Bingemer, H. and Peter, T.: Global atmospheric sulfur budget under volcanically quiescent conditions: Aerosol-chemistry-climate model predictions and validation, J. Geophys. Res. Atmospheres, 120(1), 256–276, doi:10.1002/2014JD021985, 2015.

Smith, J. P., Dykema, J. A. and Keith, D. W.: Production of Sulfates Onboard an Aircraft: Implications for the Cost and
5   Feasibility of Stratospheric Solar Geoengineering, Earth Space Sci., 5(4), 150–162, doi:10.1002/2018EA000370, 2018.

Stenke, A., Schraner, M., Rozanov, E., Egorova, T., Luo, B. and Peter, T.: The SOCOL version 3.0 chemistry-climate model: description, evaluation, and implications from an advanced transport algorithm, Geosci. Model Dev., 6(5), 1407–1427, doi:10.5194/gmd-6-1407-2013, 2013.

Stier, P., Feichter, J., Kinne, S., Kloster, S., Vignati, E., Wilson, J., Ganzeveld, L., Tegen, I., Werner, M., Balkanski, Y.,
10   Schulz, M., Boucher, O., Minikin, A. and Petzold, A.: The aerosol-climate model ECHAM5-HAM, Atmos Chem Phys, 5(4), 1125–1156, doi:10.5194/acp-5-1125-2005, 2005.

Sukhodolov, T., Sheng, J.-X., Feinberg, A., Luo, B.-P., Peter, T., Revell, L., Stenke, A., Weisenstein, D. K. and Rozanov, E.: Size-Resolved Stratospheric Aerosol Distributions after Pinatubo Derived from a Coupled Aerosol-Chemistry-Climate Model, SOCOL-AERv1.0, Geosci. Model Dev., 11, 2633–2647, doi.org/10.5194/gmd-11-2633-2018, 2018.

15   Tilmes, S., Müller, R. and Salawitch, R.: The Sensitivity of Polar Ozone Depletion to Proposed Geoengineering Schemes, Science, 320(5880), 1201–1204, doi:10.1126/science.1153966, 2008.

Tilmes, S., Richter, J. H., Mills, M. J., Kravitz, B., MacMartin, D. G., Vitt, F., Tribbia, J. J. and Lamarque, J.-F.: Sensitivity of Aerosol Distribution and Climate Response to Stratospheric SO2 Injection Locations, J. Geophys. Res. Atmospheres, 122(23), 12,591-12,615, doi:10.1002/2017JD026888, 2017.

20   Toon, O. B., Turco, R. P., Westphal, D., Malone, R. and Liu, M.: A Multidimensional Model for Aerosols: Description of Computational Analogs, J. Atmospheric Sci., 45(15), 2123–2144, doi:10.1175/1520-0469(1988)045<2123:AMMFAD>2.0.CO;2, 1988.

Weisenstein, D. K., Yue, G. K., Ko, M. K. W., Sze, N.-D., Rodriguez, J. M. and Scott, C. J.: A two-dimensional model of sulfur species and aerosols, J. Geophys. Res. Atmospheres, 102(D11), 13019–13035, doi:10.1029/97JD00901, 1997.

25   Weisenstein, D. K., Penner, J. E., Herzog, M. and Liu, X.: Global 2-D intercomparison of sectional and modal aerosol modules, Atmospheric Chem. Phys., 7(9), 2339–2355, doi:10.5194/acp-7-2339-2007, 2007.

Weisenstein, D. K., Keith, D. W. and Dykema, J. A.: Solar geoengineering using solid aerosol in the stratosphere, Atmospheric Chem. Phys., 15(20), 11835–11859, doi:10.5194/acp-15-11835-2015, 2015.

WMO: Scientific assessment of ozone depletion: 2006, Glob. Ozone Res. Monit. Proj.-Rep. No 50 World Meteorol. Organ.
30   [online] Available from: http://www.wmo.int/pages/prog/arep/gaw/ozone_2006/ozone_asst_report.html, 2008.

Yue, G. K., Poole, L. R., Wang, P.-H. and Chiou, E. W.: Stratospheric aerosol acidity, density, and refractive index deduced from SAGE II and NMC temperature data, J. Geophys. Res. Atmospheres, 99(D2), 3727–3738, doi:10.1029/93JD02989, 1994.
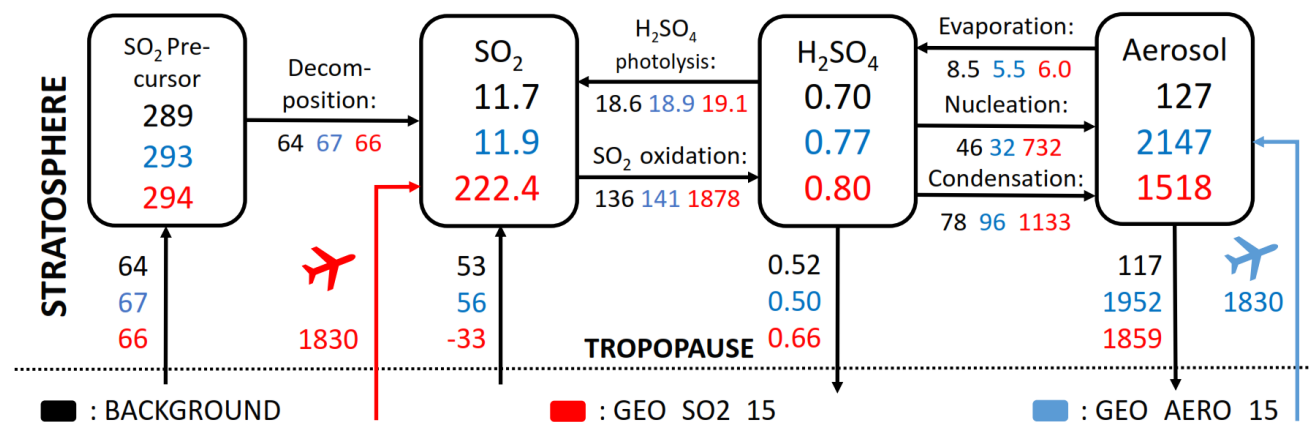
Figure 1. Schematic of the global sulfur cycle for GEO_AERO_15 (blue), GEO_SO2_15 (red), and BACKGROUND (black) averaged over the last ten years of simulations (see Table 1 for scenario definitions). Net fluxes (positive in pointing direction of arrow) are given in Gg S yr^{-1} and burden (in boxes) are given in Gg S. SO$_2$ precursor species include OCS, DMS, H$_2$S, CS$_2$, and H$_2$S. SO$_3$ as an intermediate step between SO$_2$ and H$_2$SO$_4$ is modeled but for simplicity omitted from the diagram.
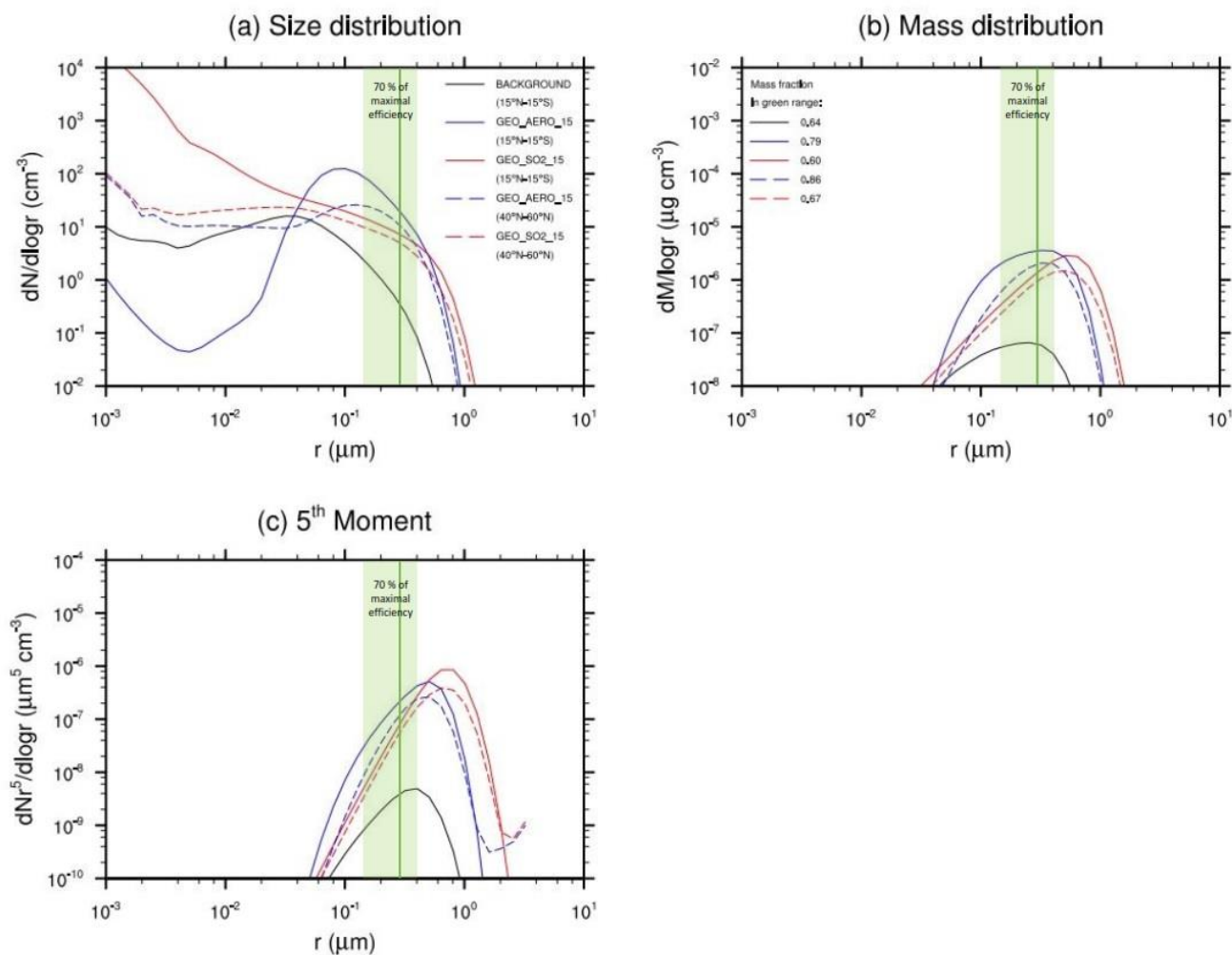
Figure 2. Size and mass distributions of stratospheric aerosol under various scenarios. **(a)** Wet aerosol size distributions of GEO_AERO_15 (blue), GEO_SO2_15 (red), and BACKGROUND (black) are zonally averaged over 10 years between 15° N and 15° S (continuous lines) and between 40° N and 60° N (dashed lines). Values shown are at 50 hPa in the tropics and at 100 hPa in the northern midlatitudes, i.e. at the levels of peak aerosol mass concentration in the vertical profile (see Fig. 3). The green size range is defined as the radius at which backscattering efficiency on sulfate aerosols is at least 70 % (i.e. 0.12-0.40 μm) of its maximal value (solid green line at 0.30 μm) following Dykema et al. (2016). **(b)** The resulting mass distributions of the size distribution curves shown in (a) including the wet aerosol mass fraction in the optimal size range between 0.12 and 0.40 μm in the legend. **(c)** The 5th moment of the aerosol size distribution shown in (a) as an estimate for aerosol sedimentation mass flux.
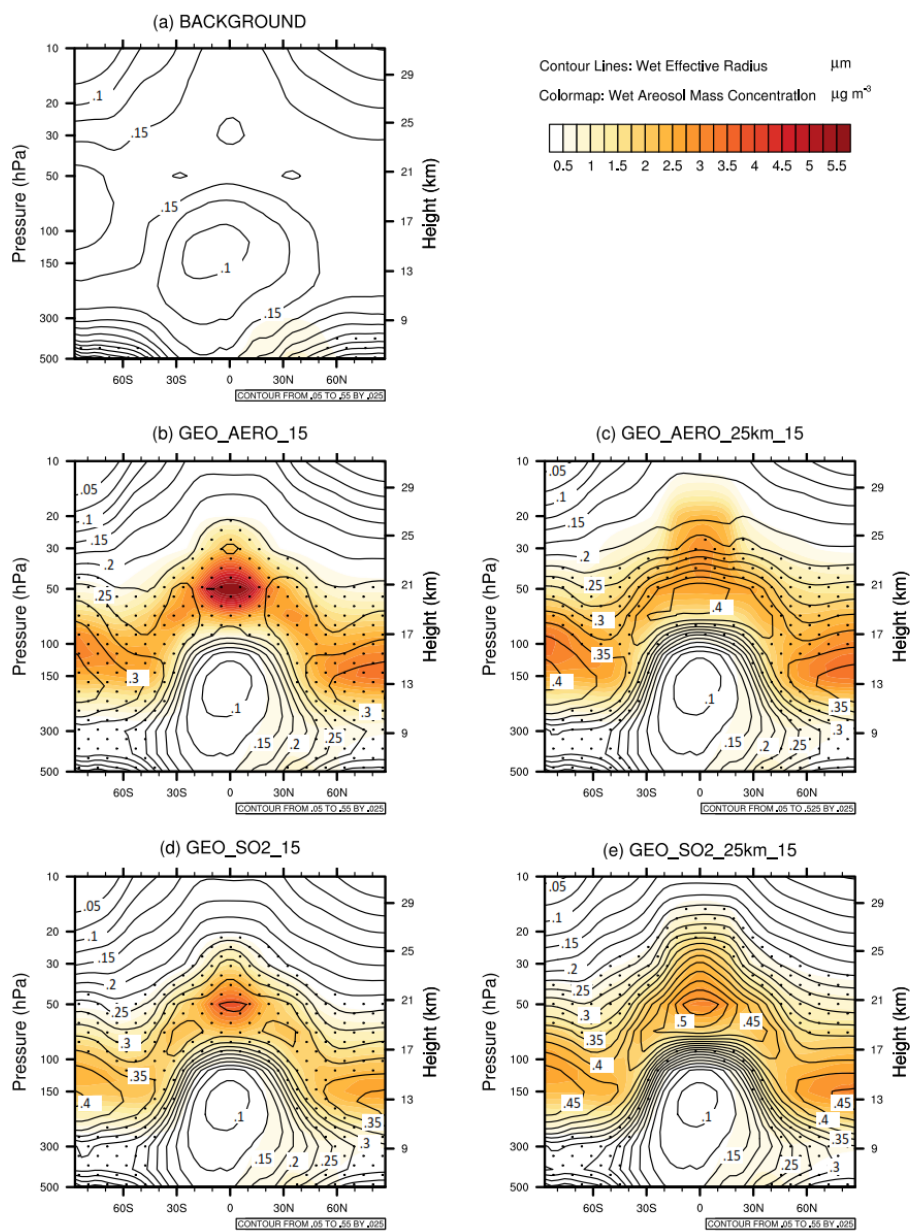
Figure 3. Contour lines show the wet effective radius (i.e. the ratio between the 3rd moment and the 2nd moment of the aerosol size distribution) in µm. The dotted area depicts the size range with effective radii between 0.24 µm and 0.36 µm. It is the range in which the backscattering efficiency is larger than 90 % of its peak value at 0.3 µm following Dykema et al. (2016). Color maps show the wet aerosol mass distribution in µg m^{-3} both zonally averaged over ten years for background conditions (**a**), GEO_AERO_15 (**b**), GEO_AERO_25km_15 (**c**), GEO_SO2_15 (**d**) and GEO_SO2_25km_15 (**e**).
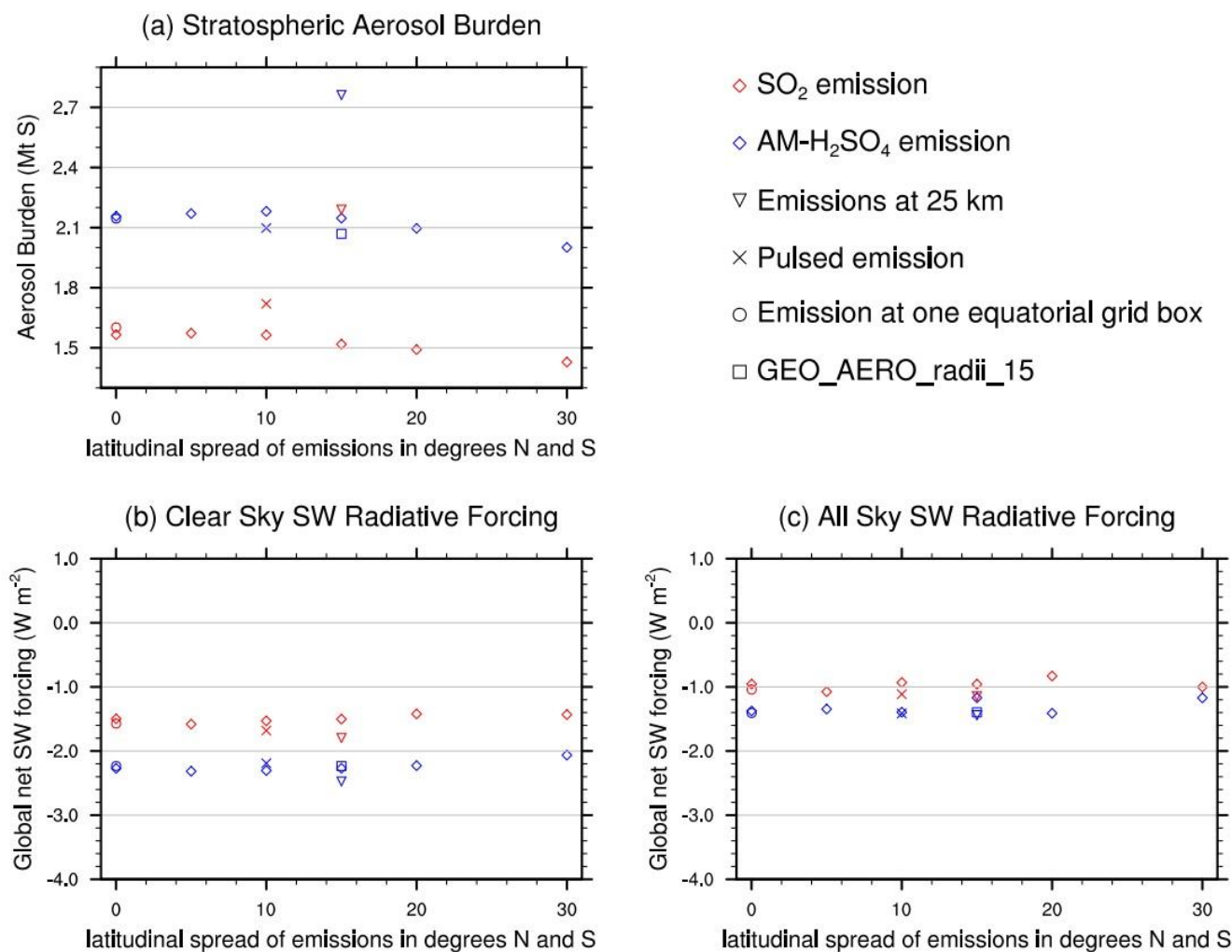
Figure 4. Globally averaged stratospheric aerosol burden **(a)**, clear sky **(b)**, and all sky **(c)** short-wave surface radiative forcing for various scenarios simulated in this study. AM-H2SO4 emission scenarios are shown in blue and SO2 emission scenarios are shown in red. Reference scenarios are shown with "diamond" symbols. Alternate cases have symbols as indicated in key.
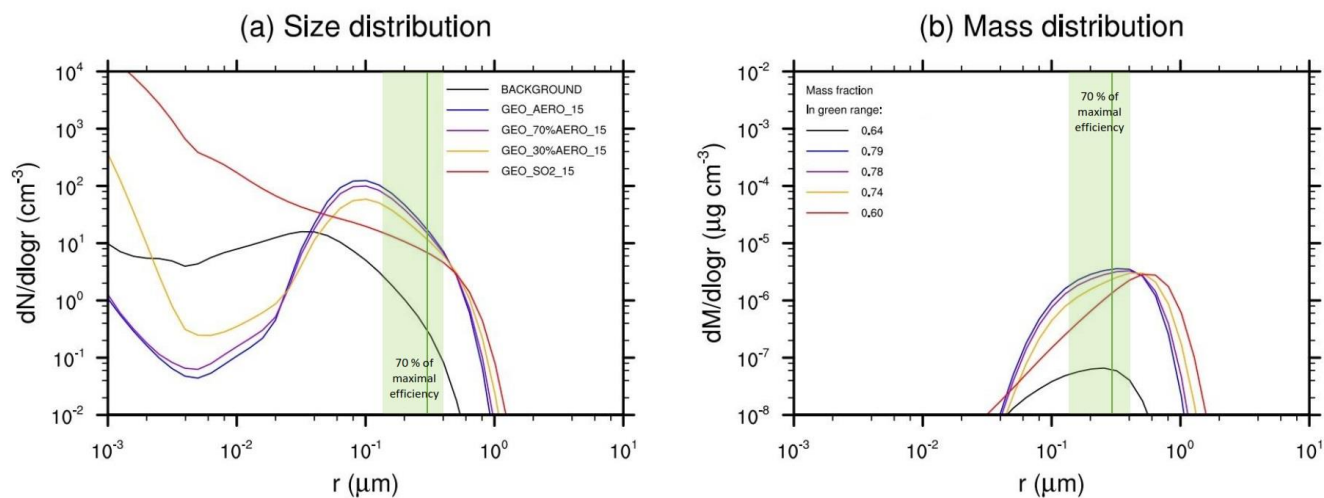
Figure 5. (a) Wet aerosol size distribution of scenarios with various emission mixtures of AM-H_2SO_4 and SO_2 averaged between 15° N and 15° S at 50 hPa. The green size range is defined as the radius at which backscattering efficiency on sulfate aerosols is larger than 70 % (i.e. 0.12−0.40 µm) of its maximal value (solid green line at 0.30 µm) following Dykema et al. (2016). **(b)** Mass distributions of the size distributions resulting from (a) including the wet aerosol mass fraction in the optimal size range between 0.12 and 0.40 µm in the legend.
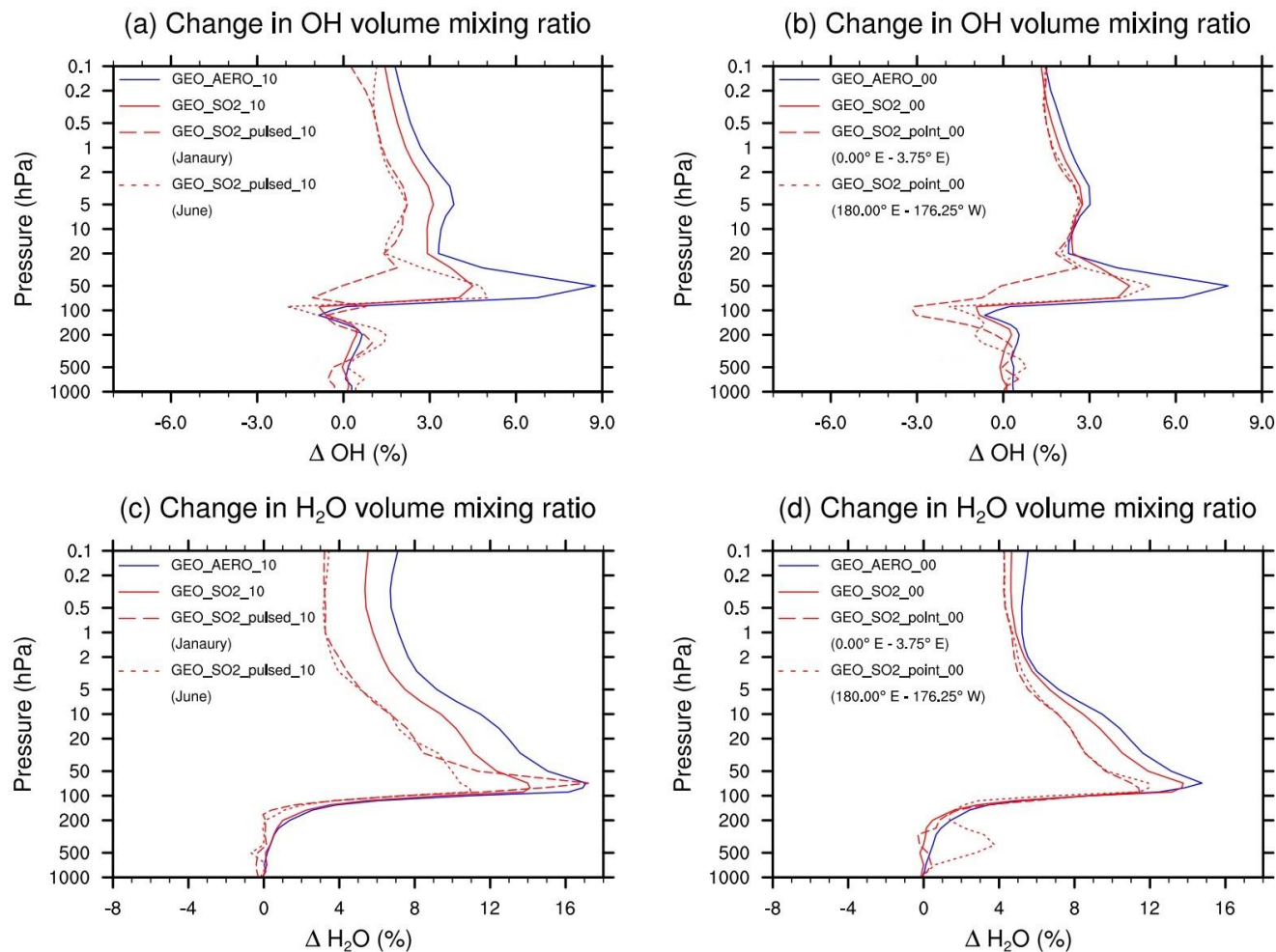
Figure 6. Vertical profile of the OH volume mixing ratio anomaly **(a and b)** and H_2O volume mixing ratio anomaly **(b and c)**. Anomalies represent prudential difference compared to the background simulation. Data show annual and zonal averages between 15° N and 15° S except where indicated. The left column **(a and c)** shows results for injections within 10° of the equator, while the right column **(b and d)** shows results for injections at the equator. For equatorial injection (right column), we also show results averaged from 0° E to 3.75° E and from 180° E to 176.25° W. For the 10° injection case (left column), we also show zonal averages of January (emissions during January 1st and 2nd) and June (month before emission) from the pulsed simulation. Note how SO_2 injection scenarios tend to reduce OH concentrations around 50 hPa compared with AM-H_2SO_4 injection scenarios (due to the reaction $SO_2+OH \rightarrow SO_3+HO_2$), while both increase stratospheric H_2O concentrations (due to warming).
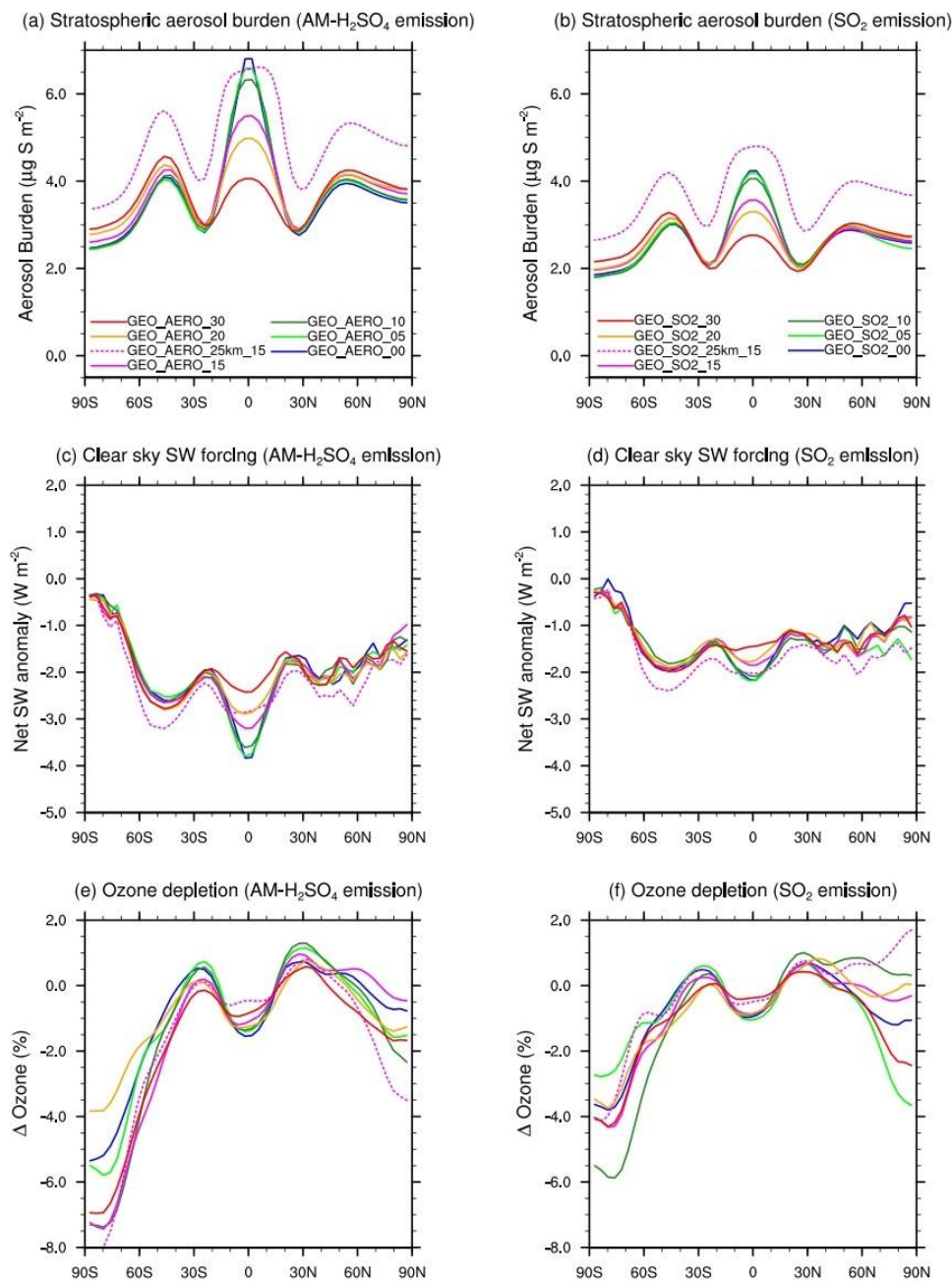
Figure 7. Zonally averaged stratospheric aerosol burden **(a and b)**, clear sky short-wave radiative forcing **(c and d)**, and depletion of the total ozone column **(e and f)** as a function of latitude for AM-H_2SO_4 **(a, c and e)** and SO_2 **(b, d and f)** emission scenarios with different latitudinal spread as well as for emissions at 25 km for comparison.

Nr	Scenario	Longitude	Latitude	H$_2$SO$_4$ (liq)	SO$_2$ (gas)	Remarks
0	BACKGROUND	-	-	0 %	0 %	reference run
1	GEO_AERO_00	0°–360° E	3.75° N–3.75° S	100 %	0 %	-
2	GEO_AERO_05	0°–360° E	5° N–5° S	100 %	0 %	-
3	GEO_AERO_10	0°–360° E	10° N–10° S	100 %	0 %	-
4	GEO_AERO_15	0°–360° E	15° N–15° S	100 %	0 %	-
5	GEO_AERO_20	0°–360° E	20° N–20° S	100 %	0 %	-
6	GEO_AERO_30	0°–360° E	30° N–30° S	100 %	0 %	-
7	GEO_SO2_00	0°–360° E	3.75° N–3.75° S	0 %	100 %	-
8	GEO_SO2_05	0°–360° E	5° N–5° S	0 %	100 %	-
9	GEO_SO2_10	0°–360° E	10° N–10° S	0 %	100 %	-
10	GEO_SO2_15	0°–360° E	15° N–15° S	0 %	100 %	-
11	GEO_SO2_20	0°–360° E	20° N–20° S	0 %	100 %	-
12	GEO_SO2_30	0°–360° E	30° N–30° S	0 %	100 %	-
13	GEO_AERO_pulsed_10	0°–360° E	10° N–10° S	100 %	0 %	two emission pulses per year (every 6 months)
14	GEO_SO2_pulsed_10	0°–360° E	10° N–10° S	0 %	100 %	
15	GEO_AERO_point_00	0°–3.75° E	3.75° N–3.75° S	100 %	0 %	emissions at only one equatorial grid box
16	GEO_SO2_point_00	0°–3.75° E	3.75° N–3.75° S	0 %	100 %	
17	GEO_30%AERO_15	0°–360° E	15° N–15° S	30 %	70 %	emission of different mixtures of SO$_2$ and AM–H$_2$SO$_4$
18	GEO_70%AERO_15	0°–360° E	15° N–15° S	70 %	30 %	
19	GEO_AERO_25km_15	0°–360° E	15° N–15° S	100 %	0 %	emission altitude = 25 km
20	GEO_SO2_25km_15	0°–360° E	15° N–15° S	0 %	100%	
21	GEO_AERO_radii_15	0°–360° E	15° N–15° S	100 %	0 %	r_m = 0.15 μm

Table 1. Overview of all simulations performed in this study. Each GEO scenario (1)-(12) assumes a zonally symmetric and continuous injection of 1.83 Mt S yr^{-1} as SO$_2$ and/or accumulation mode particles (AM-H$_2$SO$_4$) with lognormal size distribution (dry mode radius, r_m = 0.095 μm and distribution width σ = 1.5). Longitudinal and latitudinal distributions as well as emission ratios of liquid to gas (in sulfur mass) are shown in columns 3-6. GEO scenarios (13)-(20) deviate from these standard conditions as indicated under remarks.

Nr	Scenario	Aerosol Burden (Gg S)	Strat. Aerosol resid. time (months)	Clear Sky SW RF (W m⁻²)	All Sky SW RF (W m⁻²)	Clear Sky RF / All Sky RF	ΔOzone Column (%)	Tropo-pause ΔT (K)	ΔH$_2$O Volume Mixing Ratio (ppmv)	Effective Radius (r$_e$) 40° N–60° N	Effective Radius (r$_e$) 15° N–15° S
0	BACKGROUND	127	13.03	0.00	0.00	-	0.00	0.00	0.00	0.13	0.14
1	GEO_AERO_00	2156	13.25	-2.27	-1.38	1.65	-0.49	0.95	0.40	0.27	0.24
2	GEO_AERO_05	2169	13.33	-2.32	-1.35	1.72	-0.49	1.15	0.52	0.27	0.23
3	GEO_AERO_10	2181	13.39	-2.30	-1.39	1.65	-0.65	1.17	0.51	0.27	0.23
4	GEO_AERO_15	2147	13.20	-2.27	-1.17	1.94	-0.75	1.22	0.55	0.27	0.23
5	GEO_AERO_20	2096	12.87	-2.23	-1.41	1.58	-0.57	0.95	0.41	0.26	0.23
6	GEO_AERO_30	2002	12.30	-2.06	-1.17	1.76	-0.98	0.84	0.37	0.24	0.22
7	GEO_SO2_00	1565	10.36	-1.50	-0.96	1.57	-0.36	0.96	0.42	0.33	0.35
8	GEO_SO2_05	1571	10.30	-1.58	-1.07	1.47	-0.43	1.04	0.46	0.33	0.35
9	GEO_SO2_10	1564	10.16	-1.53	-0.93	1.64	-0.36	0.99	0.44	0.33	0.35
10	GEO_SO2_15	1518	9.80	-1.50	-0.96	1.57	-0.43	0.88	0.38	0.33	0.35
11	GEO_SO2_20	1491	9.61	-1.42	-0.83	1.71	-0.44	0.82	0.33	0.33	0.34
12	GEO_SO2_30	1428	9.12	-1.43	-1.00	1.43	-0.51	0.84	0.36	0.32	0.34
13	GEO_AERO_pulsed_10	2098	12.89	-2.19	-1.41	1.55	-0.69	0.74	0.35	0.28	0.26
14	GEO_SO2_pulsed_10	1720	11.62	-1.68	-1.11	1.51	-0.41	0.84	0.31	0.30	0.30
15	GEO_AERO_point_00	2145	13.18	-2.23	-1.41	1.59	-0.76	0.87	0.42	0.28	0.25
16	GEO_SO2_point_00	1602	14.24	-1.57	-1.04	1.51	-0.10	1.03	0.34	0.31	0.33
17	GEO_30%AERO_15	1829	11.55	-1.84	-1.11	1.66	-0.75	0.97	0.38	0.30	0.28
18	GEO_70%AERO_15	2010	12.52	-2.09	-1.14	1.82	-0.87	0.80	0.44	0.27	0.24
19	GEO_AERO_25km_15	2761	17.04	-2.47	-1.44	1.72	-0.82	0.72	0.30	0.34	0.39
20	GEO_SO2_25km_15	2190	13.80	-1.80	-1.22	1.48	-0.26	0.75	0.33	0.41	0.52
21	GEO_AERO_radii_15	2069	12.71	-2.23	-1.40	1.59	-0.61	0.88	0.38	0.42	0.53

Table 2. Summarized values of all quantities calculated in this study. The first four columns show total stratospheric aerosol burden, globally averaged clear sky and all sky surface short-wave radiative forcing, as well as the ratio between the globally averaged clear sky and all sky short-wave radiative forcing. For ozone depletion, globally averaged values of the total ozone column reduction are shown in percentage points. Temperature increases and H$_2$O volume mixing ratio increases are given as values averaged between 15° N and 15° S at 90 hPa (i.e. at the tropical cold point tropopause). The last 2 columns show wet effective radius averaged between 40° N and 60° N at 100 hPa and between 15° N and 15° S at 50 hPa.

Nr	Scenario	Injection Rate / ΔAll Sky SW RF	Aerosol Burden / ΔAll Sky SW RF	ΔOzone Column / ΔAll Sky SW RF	ΔH$_2$O / ΔAll Sky SW RF	ΔT / ΔAll Sky SW RF	Mass fraction 0.12—0.40 µm (40 °N—60 °N)	Mass fraction 0.12—0.40 µm (15° N—15° S)
0	BACKGROUND	-	-	-	-	-	0.59	0.64
1	GEO_AERO_00	-1.32	-1.57	0.36	-0.29	-0.69	0.87	0.80
2	GEO_AERO_05	-1.35	-1.61	0.37	-0.38	-0.86	0.87	0.80
3	GEO_AERO_10	-1.31	-1.56	0.47	-0.37	-0.84	0.87	0.79
4	GEO_AERO_15	-1.56	-1.84	0.64	-0.47	-1.04	0.86	0.79
5	GEO_AERO_20	-1.30	-1.49	0.40	-0.29	-0.67	0.86	0.80
6	GEO_AERO_30	-1.56	-1.71	0.83	-0.31	-0.72	0.86	0.81
7	GEO_SO2_00	-1.90	-1.64	0.38	-0.44	-1.01	0.68	0.60
8	GEO_SO2_05	-1.71	-1.46	0.40	-0.43	-0.97	0.67	0.59
9	GEO_SO2_10	-1.96	-1.68	0.39	-0.47	-1.07	0.66	0.59
10	GEO_SO2_15	-1.90	-1.58	0.45	-0.39	-0.92	0.67	0.60
11	GEO_SO2_20	-2.20	-1.80	0.53	-0.40	-0.98	0.67	0.61
12	GEO_SO2_30	-1.83	-1.43	0.51	-0.36	-0.84	0.68	0.63
13	GEO_AERO_pulsed_10	-1.30	-1.48	0.49	-0.25	-0.52	0.90	0.87
14	GEO_SO2_pulsed_10	-1.65	-1.54	0.37	-0.28	-0.75	0.76	0.70
15	GEO_AERO_point_00	-1.30	-1.52	0.54	-0.30	-0.62	0.89	0.85
16	GEO_SO2_point_00	-1.76	-1.54	0.10	-0.33	-0.99	0.71	0.63
17	GEO_30%AERO_15	-1.65	-1.37	0.67	-0.34	-0.88	0.79	0.74
18	GEO_70%AERO_15	-1.60	-1.76	0.76	-0.38	-0.69	0.85	0.78
19	GEO_AERO_25km_15	-1.27	-1.92	0.57	-0.21	-0.50	0.84	0.77
20	GEO_SO2_25km_15	-1.50	-1.80	0.21	-0.27	-0.61	0.58	0.41
21	GEO_AERO_radi_15	-1.31	-1.48	0.44	-0.27	-0.63	0.90	0.88

Table 3. Comparison of important impacts normalized to the all sky short-wave radiative forcing. The smaller the absolute value of the ratio, the smaller the injection rate or impact to achieve a given level of radiative forcing. For each column, the smallest/largest three absolute values are marked in green/red. Columns show globally averaged values of sulfur injection rate, resulting stratospheric aerosol burden and ozone depletion, as well as H$_2$O volume mixing ratio increase, and temperature increases at the tropical cold point tropopause (i.e. at 90 hPa) normalized to the resulting all sky short-wave radiative forcing. Last two columns show the wet aerosol mass fraction in the range between 0.12 and 0.40 µm of the resulting size distribution. The three largest mass fractions are marked in green and the three smallest mass fractions are marked in red.